CERN-ACC-NOTE-2019-0037
xavier.buffat@cern.ch

Studies of PACMAN effects in the HL-LHC

A. Ribes-Metidieri, X. Buffat, CERN, Geneva, Switzerland

Abstract

This note summarises the status of the studies on PACMAN beam-beam effects in the HL-LHC project. It is shown that the orbit, tune and chromaticity effects due to head-on and long-range beam-beam interactions are tolerable without dedicated mitigations in the nominal scenario. Nevertheless, the orbit effects are not negligible when considering the tolerance for the asynchronous beam dump. Thus, an adjustment of the required apertures is suggested. The luminosity loss due to the PACMAN orbit effects is shown to be negligible in the high luminosity experiments and tolerable in the low luminosity ones. The single particle stability is also briefly discussed, showing that it would be interesting to perform further studies on dynamic aperture taking into account the offsets at the IPs induced by orbit effects due to the strong chromaticity introduced in the presence of residual dispersion at the interaction point. The concept of PACMAN linear coupling is introduced and implemented in the code TRAIN. This effects imposes tight tolerance on the alignment of the crossing angles, thus a procedure for experimental validation at the LHC is proposed.

Geneva, Switzerland
September 19, 2019

Contents

1 Introduction

The high luminosity upgrade of the LHC, the HL-LHC, relies on several factors that tend to increase the strength of beam-beam interactions such as a lower β^* and an increase of the bunch population. The bunch to bunch differences introduced by missing beam-beam interactions, so-called PACMAN effects, were well studied for the LHC and do not affect its performance [1, 2]. Here we assess the orbit effects, tune shifts, and chromaticity shifts for the HL-LHC, with emphasis on the impact on the physical aperture requirements, crab cavity loading, single particle stability and coherent stability of the beam. We also introduce the new concept of PACMAN linear coupling driven by skew long-range beam-beam interactions.

This analysis will be carried on with the self-consistent code TRAIN, adapted to the HL-LHC layout and optics. Unless stated otherwise, all studies are based on the baseline parameters detailed in [3].

1.1 Beam-Beam coherent interactions

The HL-LHC will collide particles of the same type travelling in separate beam pipes all around the machine except in four interaction regions, where the experiments are installed. The beams share a common vacuum chamber in these four locations over more than 240 m. Due to the presence of a small crossing angle, the bunches will not meet head-on during all their trajectory along the common chamber as represented in Fig. 1. Long-range electromagnetic interactions will take place all along the trajectory of both beams. As it can be appreciated in Fig. 1, the whole common chamber is not a drift space, but contain several magnets that bend the beam trajectory in order to allow the collision at the Interaction Point (IP). In Fig. 1, the positions of the dipoles D1 and D2 have been indicated on the reference orbit (in dashed black line), so it can be appreciated how D2 bends beam 1 and 2 in the plane perpendicular to the crossing angle to conduct the beams inside the beam pipes while D1 separates both beams

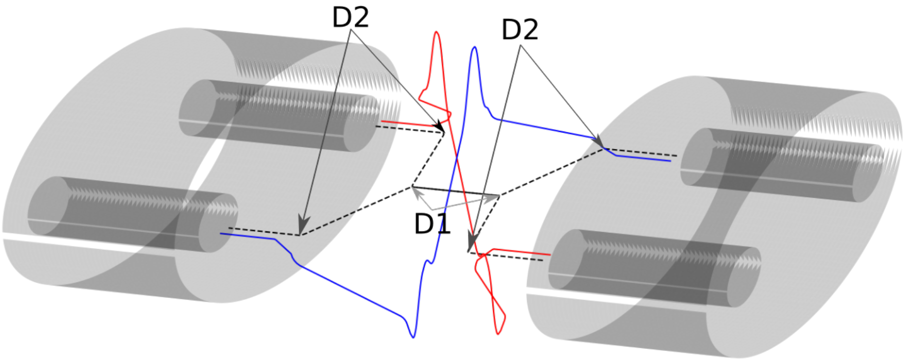

Figure 1: Schematic representation of the interaction region 5 with beam 1 in blue and beam 2 in red. In the vertical plane we observe the crossing angle and in the horizontal one, the separation bump between both beams. In black, the reference trajectory is represented. The presence of the dipoles D1 and D2 is also indicated in the reference trajectory, so the effect of D1 and D2 on the reference orbit may be appreciated. The inner triplet, located between the dipoles D1, is the responsible of focusing the beams in the IP.

outside of the drift space between both D1. As opposed to IP5, the crossing angle bumps adds to the reference orbit in the horizontal plane around IP1. The final focusing of the proton beams before collision is achieved through the inner triplet, formed by three quadrupoles located between the D1 dipoles.

The electromagnetic interaction of the bunches of both beams manifests itself as a deflection, or kick, of every particle in the other beam. Since this kick varies strongly for particles oscillating at different amplitude, it is convenient to define the averaged kick over the beam distribution, known as the coherent beam-beam kick. The coherent kick that a round Gaussian distribution of particles induces in the opposing beam's centroid is obtained by the integration of the single-particle kicks over the beam distribution [4]

$$\Delta x'_{coh}(x,y) = -\frac{2r_p N}{\gamma_r}\frac{x}{r^2}\left(1-e^{-r^2/4\sigma^2}\right) \tag{1}$$

with $r=\sqrt{x^2+y^2}$, r_p the classical proton radius, N the number of charges in the bunch, σ the r.m.s. beam size and γ_r the relativistic gamma factor. The transverse positions in the horizontal and vertical planes, x and y, are relative to the centre of the opposing beam.

The coherent kick will result in a modification of the closed orbit. Considering the orbit effects of both beams self-consistently, the following equations can be derived [4]

$$\delta x_1 = \Delta x'_{coh}(d+\delta x_1+\delta x_2)\beta_1 \cot(\pi Q_1) \tag{2}$$

$$\delta x_2 = \Delta x'_{coh}(d+\delta x_1+\delta x_2)\beta_2 \cot(\pi Q_2) \tag{3}$$

where d stands for the distance between the orbit of the two beams, β_i is the optical β function of beam i at the location of the interaction, and Q_i is the unperturbed tune for beam i. Equations 2 and 3 could be used in order to estimate the orbit distortions of both beams if the beams were formed by a uniform sequence of bunches. However, the non-uniform filling of the machine leads to the so called PACMAN effect.

1.2 PACMAN effect

Due to the finite rising time of the injection kickers in the different machines composing the injection chain, the bunches are injected along the 3564 available RF buckets with a filling scheme composed of trains of consecutive bunches spaced by 25 ns, interleaved with empty gaps. The largest gap at the end of the beam allows for the rise of the dump kicker in the LHC, known as the abort gap. If the filling scheme featured a 4-fold symmetry and the machine layout an 8-fold symmetry, all bunches would interact in all IPs. However, because of the introduction of the abort gap and the slight displacement of the IP8 (LHCb) by three RF slots, these symmetries are broken. As a result, some bunches of both beams are missing beam-beam interactions. The usual impact of beam-beam interactions on the beam dynamics such as closed orbit and optics distortions (tune, chromaticity or even linear coupling) becomes different for each bunch and can no longer be corrected with a global correction system. The bunches missing long-range or head-on interaction are often referred to as PACMAN and super-PACMAN bunches respectively.

We may expect that PACMAN effects impact the performance of HL-LHC in the following ways. The PACMAN orbit effects will produce an offset between the beams at the IPs, yielding a luminosity reduction. The orbit spread may represent a limitation in terms of physical aperture and generate beam loading in the transverse deflecting cavities. Moreover, the changes in tune and chromaticity produced by the PACMAN effects may also reduce the beam lifetime. Finally, coherent instabilities may result from the reduction of Landau damping caused by uncorrected linear coupling. In the following, we will analyse the impact of those effects for HL-LHC in order to identify possible performance limitations.

Using the map formalism, the closed orbit is defined as the first-order fixed point of a non linear equation of type

$$\bar{x}_{i,j,k+1} = M_i(\bar{x}_{i,j,k}) \tag{4}$$

with M_i the one-turn map of beam $i = 1,2$, $\bar{x}_{i,j,k}$ the 6D coordinates of bunch j of beam i at turn k. If we introduce the effect of the beam-beam interactions, the dimensionality of the problem is increased, since each bunch will experience a different closed orbit depending on the number of beam-beam interactions that it is receiving. The one-turn maps for bunch j of beam i with beam-beam interactions $M'_{i,j}$ will be split into maps where the interactions take place and thus we have introduced the beam-beam coherent kicks

$$M'_{i,j} = \prod_{l}^{N_{BB}} M_{i,l} M^{BB}_{i,j,l}, \quad M^{BB}_{i,j,l} : x'_{i,j} \to x'_{i,j} + \Delta x'_{coh}(x_{i,j} - x_{S(i,j,l)}, y_{i,j} - y_{S(i,j,l)}) \tag{5}$$

with $M^{BB}_{i,j,l}$ the non-linear beam-beam map of beam i,bunch j at location l and $S(i,j,l)$ the bunch index of the other beam colliding with beam i and bunch j at the IP l and $M_{i,l}$ the map of beam i between interaction l and $l+1$.

1.3 Weak-strong approach vs strong-strong approach

In order to obtain the closed orbits of all bunches solving Eq. 4 including the beam-beam interactions using Eq. 5, we can use the weak-strong approximation, in which we treat the beam-beam interactions as a static lens and assume that a "weak" beam (a single particle) is perturbed by a "strong" one which is assumed to be static. In other words, Eq. 4 is split into two separate problems, with $i = 1$ or $i = 2$. However, when the beam-beam perturbation is important the weak-strong model is not any longer valid, since both beams change their closed orbit self-consistently, so we must apply a self-consistent approach, often called strong-strong approach. In Fig. 2, we show the result of analysing the maximum root mean square of the orbit offsets of the different bunches and the maximum peak to peak orbit offset, the tune spread and the chromaticity spread for both the weak-strong approach and the strong-strong approach. Beam 2 is considered to be the weak beam, so in the weak-strong approach, a nominal value of bunch population for beam 2 has been set at $n = 0.023 \cdot 10^{11}$ protons per bunch, while the bunch population of beam 1 varies from $0.023 \cdot 10^{11}$ to $5 \cdot 10^{11}$ protons per bunch. During the operation cycle, bunches of $2.3 \cdot 10^{11}$ protons will be expected for both beams. The analysis has been carried on at the beginning of the process collapsing the separation bumps of IPs 1 and 5 for the ultimate scenario of the HL-LHC with the standard filling scheme [3].

As it can be seen in Fig. 2 a and b, the self consistency is not relevant in the case of the orbit, since the variation in root mean square and maximum peak to peak orbit effect is inferior to 3% for the bunch intensities that are going to be used in HL-LHC with respect to the case where the self-consistency has been contemplated. However, using the weak-strong approximation, we are underestimating the tune and the chromaticity by up to a 30 % and 20% respectively, which may be relevant.

2 TRAIN algorithm

TRAIN solves a multivariate and non-linear fixed point problem in order to find the closed orbit of all bunches in both interacting beams once the filling scheme and the beam-beam interactions have been considered.

TRAIN was developed to address PACMAN effects in LEP [5] and it was used in the LHC to explain observations of orbit effects [1, 2, 6, 7].

The code has been updated for the usage of HL-LHC and the improvements and detailed functioning can be found in [8]. In the first step, TRAIN updates the information of the Twiss parameters and the map files obtained with the program MAD-X of a single bunch in beam 1 and in beam 2 along the desired optics selected for HL-LHC (we have used the optics version HLLHC1.3 and the nominal and ultimate operational scenarios detailed in [3], unless specified otherwise). Secondly, TRAIN assembles the filling scheme information with the Twiss files in order to determine the collision of all the bunches of beam 1 with the ones of beam 2, as schematically showed in Fig. (3), and builds the corresponding one-turn map with beam-beam interactions (Eq. 5).

Then, the closed orbits of beam 1 and beam 2 without beam-beam interactions are initialized using the first order one-turn map as in Eq. 4, where the first order beam-beam map M_i for beams 1 and 2 ($i = 1,2$) has been computed concatenating the first-order sector maps $M^S_{i,l}$

$$M_i = \prod_{l}^{N_{maps}} M^S_{i,l} \tag{6}$$

that relate the coordinates of a bunch at a certain position in the ring s_1 with its coordinates at a different location s_2. In the case of TRAIN, the sector maps transport the coordinates of the bunches between the location of the long-range and head-on interactions as well as between the extra elements that can be introduced. The first and second order sector maps are used as inputs in TRAIN and have been computed using MAD-X.

Next, the program computes the beam-beam interaction maps $M^{BB}_{i,j,l}$ and introduces them in the one-turn map Eq. 5 in a self-consistent way, i.e., a double loop iteration starts. In the inner loop the closed orbit with fixed beam-beam kicks are found and in the outer one the bunch positions are updated until the convergence of both closed orbits into a stable solution. The last step is the tracking of every bunch pair with the second order maps in order to find out their orbit at predefined locations, tune, chromaticity and dispersion.

3 PACMAN effects in the HL-LHC

3.1 Orbit effects

The coherent beam-beam kicks (Eq. 1) of the long-range interactions distort the orbits of the individual bunches. Using the weak-strong approach, it can be found that the orbit distortion around the location of the kick ($s = 0$) is given by [9]

$$\Delta x(s) = \frac{N_{LR} N r_p}{d \sin(\pi Q)} \sqrt{\frac{\beta(s)}{\gamma_r \varepsilon}} \cos(|\phi(s)| - \pi Q) \tag{7}$$

$$\text{or} \quad \frac{\Delta x(s)}{\sigma} = \frac{N_{LR} N r_p}{d \varepsilon \sin(\pi Q)} \cos(|\phi(s)| - \pi Q) \tag{8}$$

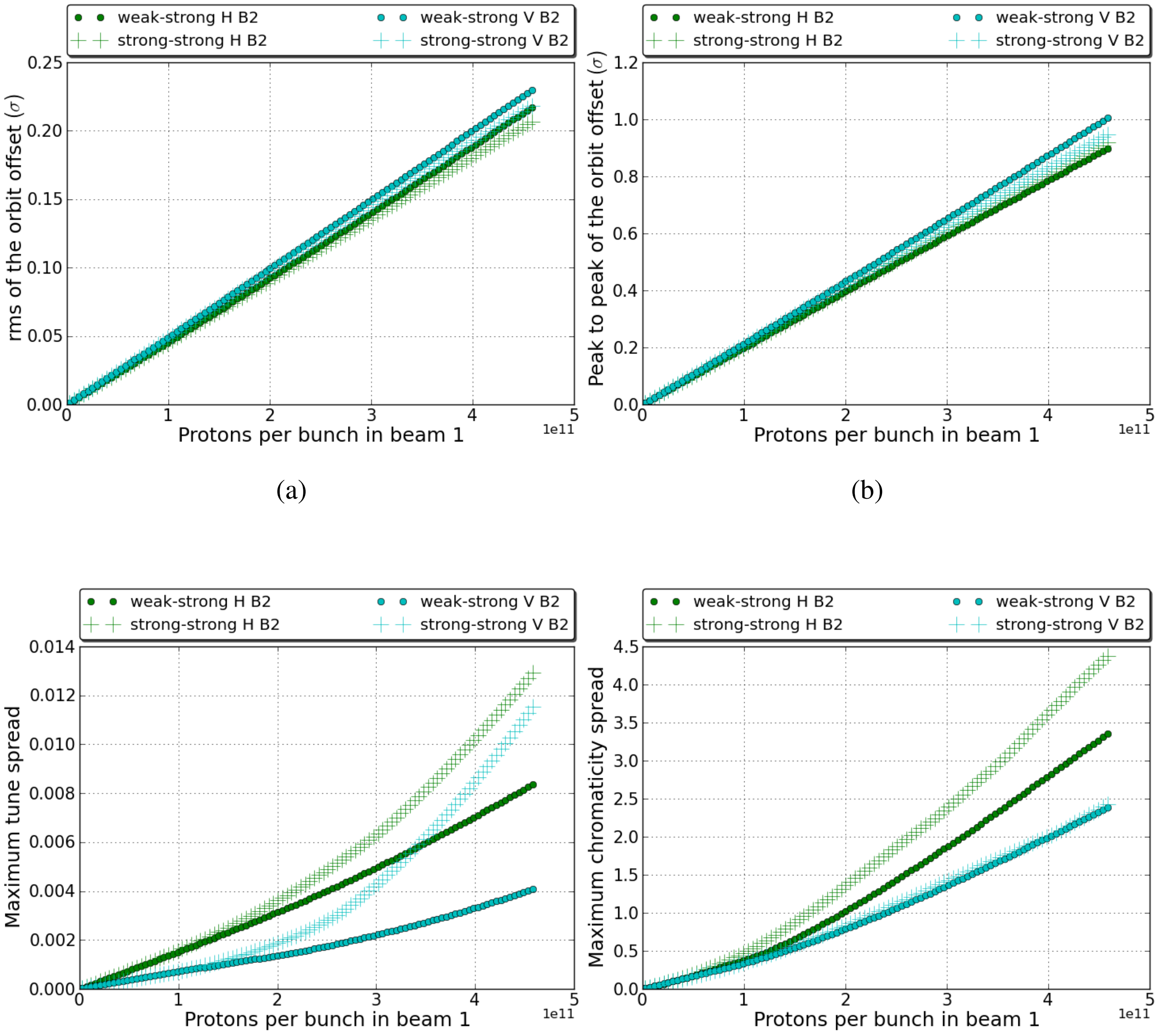

(a) (b)

(c) (d)

Figure 2: Comparison of orbit, tune and chromaticity effects within the weak-strong and strong-strong models. For the weak-strong configurations, B1 is considered as the strong beam, the results for the weak beam, i.e. B2, are shown. These results have been obtained for the ultimate scenario with collision optics ($\beta^* = 41$ cm) and the standard filling scheme [3]. For HL-LHC the current number of protons per bunch during collision is $2.2{\cdot}10^{11}$.

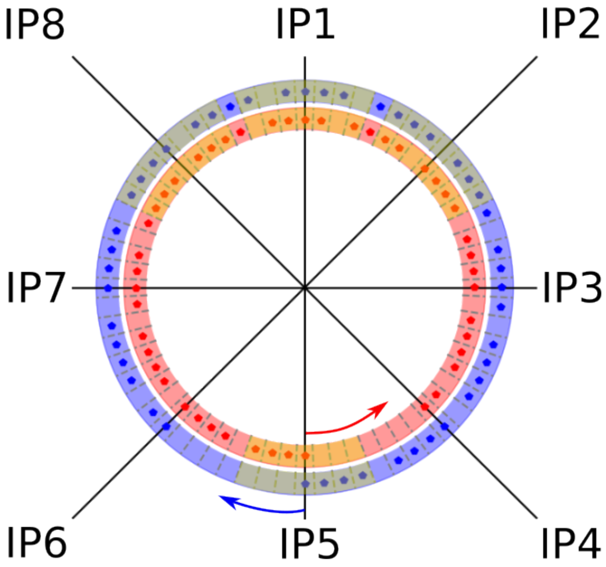

Figure 3: Schematic representation of the HL-LHC with the four IPs 1,2,5 and 8. The buckets are marked with red and blue boxes and the bunches are represented by blue and red dots. The information of the Twiss files has been used to build the interaction regions up to D2 around the IPs, marked in yellow. The filling schemes are placed anti-clockwise for beam 1 (blue) and clockwise for beam 2 (red), i.e. for both beams the description of the schemes start with the bunches at the head of the beam.

with $\beta(s)$ the optical beta-function and $\phi(s)$ the corresponding phase advance, N_{LR} the number of long-range interactions up to D1, ε the normalised emittance and Q the machine bare tune. The normalised distance d is assumed to be constant up to the separation dipole D1, and can be approximated by

$$|d| = \sqrt{\frac{\beta^* \gamma_r}{\varepsilon}}\theta \tag{9}$$

with β^* the corresponding optical function at the IP and θ the full crossing angle between the beams. This approach is not self-consistent, nevertheless, as discussed in Sec. 1.3, it is a valid approximation in the parameter range of interest. These equations also assume that the normalised distance between all bunches is constant around the IP, approximation that only holds up to D1, as it can be appreciated in Fig. 4, since the normalised distance between both beams increases rapidly between D1 and D2. The effect of the triplets is not taken into account here, it is visible in Fig. 4 via to the bumpy shapes in the normalised distance between the separation dipoles D1. However, the change of β function is considered as in a drift space. Actually, Eq. 7 is for one set of long-range interactions (right side), so the π-phase advance should be taken into account when adding the two sides, as it has been done in Fig. 5.

In Fig. 5, Eq. 8 has been represented around the IP, where the phase advance changes approximately by π, due to the strong focalisation of the β-function in this region. The closed orbit deviation for those bunches experiencing the long-range interactions at right and left of the IP have also been represented. As it can be appreciated in Fig. 5, the bunches exposed to the long-range interactions only at the left or only at the right of the IP have a different orbit deviations at the IP. The bunches of the core of the train do not miss any long-range interaction, so the orbit deviation that they will experience can be obtained by adding the effects of the long-range interactions at each side of the interaction region, as it can be also observed in Fig. 5. Also, the absolute value difference between the orbit deviation from the head to the tail or from the core to both the head and tail (in case that the orbit deviation is the same for the head and the tail, as it happens outside of the IP) is a measure of the spread of the bunches within the train and it is maximum at the IP. According to Eq. 7, the maximum normalised orbit spread is achieved

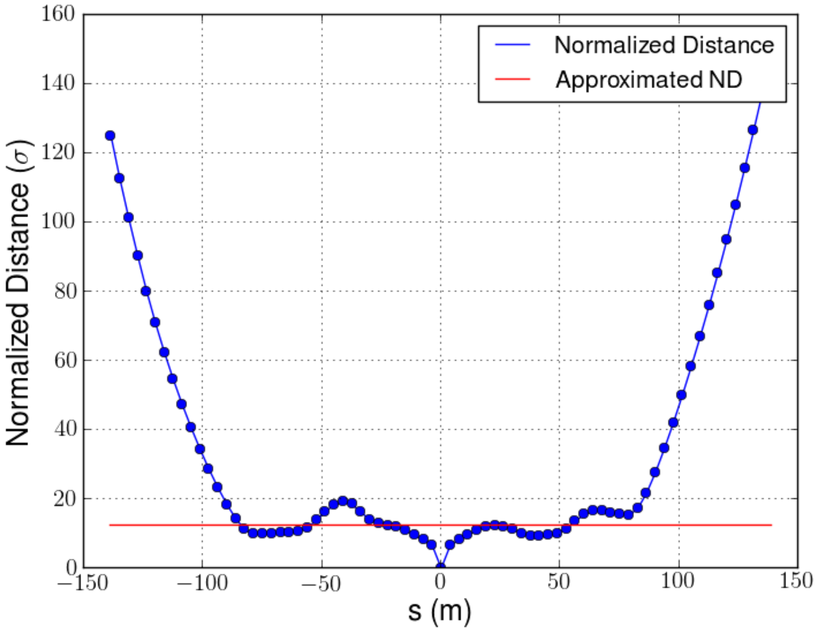

Figure 4: Normalized distance between the bunches of both beams around IP1 at the location of each long-range interactions based on the optics obtained with MAD-X in blue and the constant approximation (Eq. 9) in red. The approximated normalised distance shows a good agreement with the real normalised separation up to D1. A fast increase of the normalised distance can be appreciated from D1 to D2 and the presence of the triplets can be inferred due to the bumpy shapes in the normalised distance between the IP and D1.

in all the locations s where the phase advance satisfies $\phi(s) = \left(\frac{n}{2} - Q\right)\pi$, so the maximum normalised peak-to-peak orbit spread around the whole accelerator can be calculated as

$$\max_s \left(\frac{\Delta x(s)}{\sigma(s)}\right) = \frac{N_{LR} N r_p}{d\varepsilon \sin(\pi Q)} \tag{10}$$

and it is also shown in Fig. 5, using a discontinuous black line. Using the parameters of HL-LHC, we obtain a maximum peak-to-peak normalised orbit distortion between 0.17 and 0.22 σ from IPs 1 and 5 for the nominal and ultimate configurations at the start of collision. We note that the contributions of the two IPs do not add up since they occur in their respective crossing angle plane.

As it has been discussed, the orbit distortions that a given bunch experiences in the IPs are determined by the number of long-range and head-on interactions that it is receiving, as well as by the phase advance of the given bunch that is experiencing the coherent kick. In Fig. 6, an example of the orbit distortion as a function of the RF bucket number (also called slot id) is shown for both planes in IP1 and all bunches arranged according to the Standard filling scheme [3]. In the considered configuration and optics during collision for the nominal HL-LHC configuration[3], the total crossing angle at IP1 is considered to be horizontal with a magnitude of 500 μrad. The presence of the crossing angle introduces a different behaviour in the horizontal and vertical plane, as it can be observed in Fig. 6. For instance, the S-like shapes that can be appreciated in Fig. 6a for both beams show an interaction between both beams driven by the presence of the crossing angle in the plane of the interaction, in this case, the horizontal one. Comparing with Fig. 5, the bunches at the beginning of the train are receiving all the kicks at the right of the IP, and thus, at the IP (null phase advance) experience a positive orbit shift over the global positive beam offset due to the interactions at the two side experiments. The bunches at the tails of the train are only receiving the interactions at the left of the IP, thus presenting a negative orbit distortion, also visible in Fig. 6. Finally, the bunches at the core of the trains are receiving the same number of

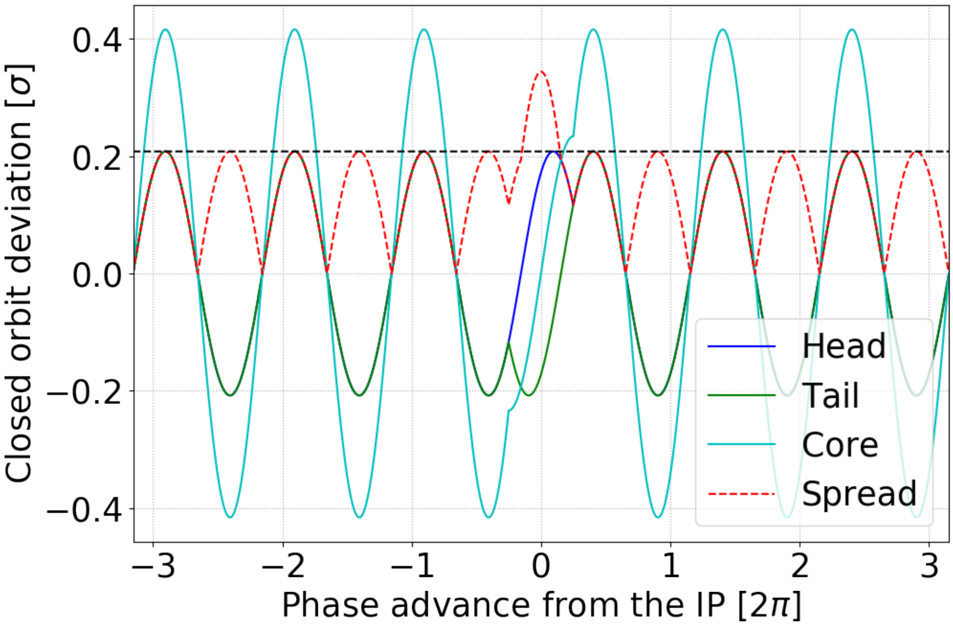

Figure 5: Normalised orbit change due to 22 long-range beam-beam interactions at 17.3 σ and at a phase advance of $\pi/2$ on each side of the IP, for an intensity of $2.2 \cdot 10^{11}$ protons per bunch and a transverse emittance of 2.5 μm, corresponding to the ultimate scenario at the start of collision. The bunches at the head and tail experience the long-range interaction only on one side of the IP, whereas the ones in the core of the train experience all of them, resulting in a non-correctable peak-to-peak orbit spread shown in dashed red. This spread is maximum at 0, i.e. at the IP. The dashed black line corresponds to Eq. 10.

positive and negative orbit distortions, resulting in a compensation of the orbit distortion at the IP, so the centre of the trains remain flat on top of the overall shift of the beam at the IP due to the head-on interaction. All intermediate bunches between the head and tail and the core are missing some of the long-range interactions at the left or right of the IP, thus presenting an intermediate orbit distortion that gives place to the continuous S-like shapes already mentioned. Since the crossing angle is unavoidable in order to maximize the luminosity, these S-like shapes are uncorrectable. On the contrary, the patterns formed in Fig. 6b, in the plane perpendicular to the crossing angle with respect to the other IPs depend mainly on the phase advance and can be reduced or even eliminated, since these M-like shapes come from the effect of the other IPs over the one that we are studying. Also in Fig. 6, two special sets of bunches from slots 800 to 990 and from 2590 to 2770 may be highlighted. These bunches experience not only missing long-range interactions following the same pattern as the other bunches, but also the head-on interactions at IP2 and IP8 due to the non-perfect fourfold symmetry of the filling scheme and the slight displacement of IP8 (LHCb). These bunches are the so-called super-PACMAN bunches and their orbit displacement depends on whether a given bunch is missing the head-on interaction in IP2, IP8 or both.

In order to provide a useful estimation of the impact of the PACMAN effects on the machine we need to define an informative estimator that allows to compare the effect in different scenarios and for different configurations, since the bunch-by-bunch orbit differences don't allow to provide a unique and significant orbit deviation sample for the whole beam, i.e., the orbit deviation of an arbitrary bunch change for different filling schemes. As we have seen in Fig. 6, in terms of orbit effects, we observe mainly two contributions, an offset of the whole beam at the IP and an orbit spread due to the different closed orbits at which different bunches circulate. Since the HL-LHC allows to re-optimize the orbit in order to correct this global offset, we will be mainly interested in defining an estimator that characterizes the spread within a beam, since the lack of a bunch-by-bunch correction method prevents us from

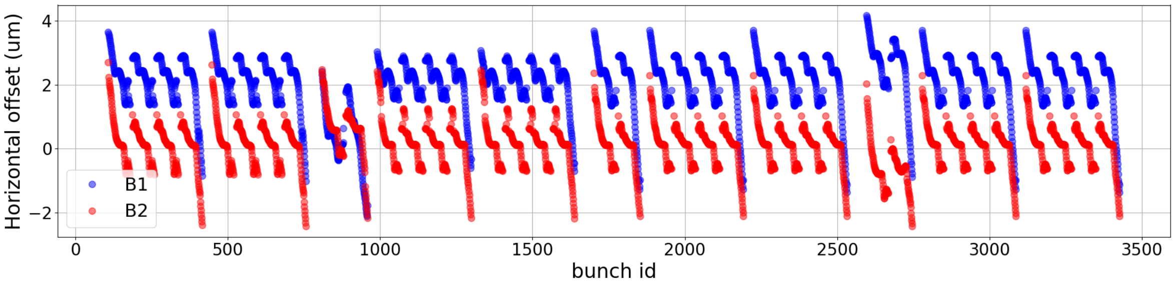

(a) Horizontal plane.

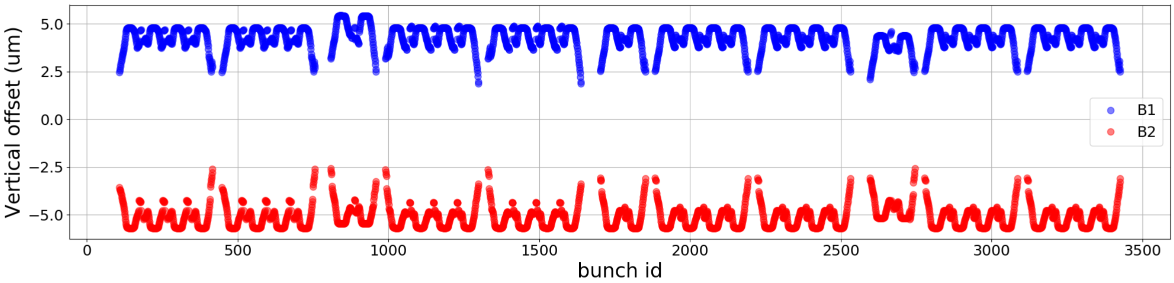

(b) Vertical plane.

Figure 6: Horizontal and vertical orbit offset at IP1 as a function of the bunch slot for the ultimate scenario at the start of collision ($\beta^* = 41$ cm) using the standard filling scheme.

correcting it. In order to characterize the spread within a beam we can consider two different estimators: the peak-to-peak orbit spread and the r.m.s. orbit spread. We may anticipate that the first one will be specially useful while discussing the effect of the orbit on the required aperture, while the r.m.s. is more representative when considering the luminosity loss. As it will be seen in Sec. 3.1.1 the impact of PACMAN effects on the luminosity is negligible and so, we will use the peak-to-peak orbit spread estimator unless stated otherwise.

As there are several sources with different phase advances, defining a global estimator of the maximum orbit spread along the whole accelerator would be quite involved, as the orbit of all bunches have to be evaluated with a fine spacial resolution. We therefore restrict ourselves to the estimation of the peak-to peak orbit spread at the IPs, which remains representative of the general behaviour in the different operational phases of the cycle, as the phase advances are constant. Figure 7 shows that the orbit spread is already significant at injection due to long-range interactions. Their contribution reduces during the ramp and increases again during the squeeze, following the corresponding increase and reduction of the normalised separation between the beams (Eq. 9). An additional contribution

Figure 7b shows that during collision the peak-to-peak orbit spread in IP1 is around 0.5 σ for both beams, corresponding to the 5 μm shown in Fig. 6a. We can estimate the orbit spread using the analytic formula Eq. 7 with a discrepancy inferior to 20%, compatible with the approximations that have been already mentioned. For instance, using Eq. 7 we obtain a Δx of 6.8 μm at IP1 during collision and 106.0 μm at injection for the nominal scenario.

With this analysis we conclude that the estimates from the TRAIN code are compatible with analytical estimates and that the amplitude of the uncorrectable orbit spread may potentially affect the luminosity and the required physical aperture for the beam, these two aspects are further detailed in the next sections.

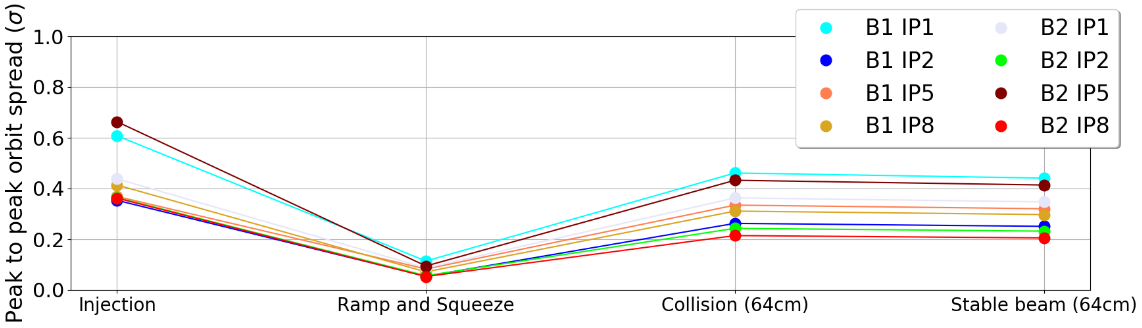

(a) Nominal operational cycle.

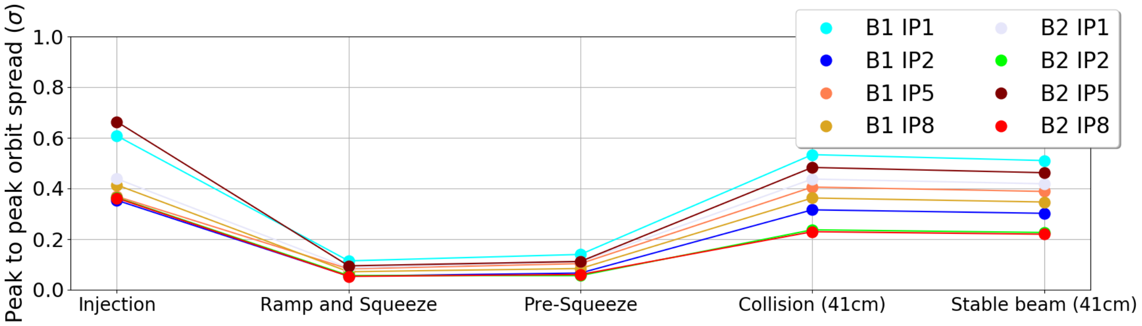

(b) Ultimate operational cycle.

Figure 7: Peak to peak orbit spread during the main phases of the nominal and ultimate operational cycle using the Standard filling scheme for the crossing angle plane in the corresponding IPs. For the IPs 1 and 8 the crossing angle plane is taken to be the horizontal one while for the IPs 2 and 5 the vertical one is considered.

3.1.1 EFFECT ON THE LUMINOSITY

We report in Figs. 8 and 9 the predictions for the luminous centroid displacement for the nominal and ultimate scenarios with collision optics at the different experiments using the Standard filling scheme and the beam parameters specified in [3] for these configurations. Since TRAIN does not allow to correct the orbit offset at the IP, but the orbit can be re-optimized during the experiments until the offset at the IP is minimum, we have post processed the data of the orbit to correct the offset following the example of [1]. The changes in the orbit resulting from the optimization of the offset at the IP are negligible, so the post processing of the data remains accurate.

In Figs. 8 and 9 the S-shapes described in Sec. 3.1 are also appreciable in the crossing angle plane for IPs 1 and 5 (horizontal and vertical respectively), and show that the luminous centroid displacement in the crossing angle plane for IP1 and 5 is mainly driven by the beam-beam interactions in that interaction region. On the contrary, the M-like shape of the luminous centroid displacement that dominates on IPs 2 and 8 indicates that the dominating contribution to the luminous centroid displacement comes from the effect of the other interaction regions on the one that we are observing, compatible with the fact that the long-range interactions are strongest in the two high luminosity IPs. As a result, the displacement of the luminous region in IPs 2 and 8 could be mitigated by adjusting the phase advance with respect to IPs 1 and 5. However, in IPs 1 and 5, the luminous centroid displacement can only be reduced by reducing the strength of the long-range interactions, for instance, by increasing the crossing angle.

Also, the relative displacement of the two beams at the IP due to collisions in other interaction regions which is in the order of 0.2 σ, corresponding to 2-3 μm, has a negligible impact on the average luminosity loss factor as shown by the estimations in Tab. 1. In our analysis we assume that the crab cavities compensate fully the effect of the crossing angle at the IP. This approximation allows to compute the luminosity loss analytically [10]

$$\frac{\Delta\mathcal{L}}{\mathcal{L}_0} = 1 - \exp\left(-\frac{\delta x^2}{4(\sigma_{1x}^2+\sigma_{2x}^2)} - \frac{\delta y^2}{4(\sigma_{1y}^2+\sigma_{2y}^2)}\right) \tag{11}$$

with δx and δy the relative displacement of the centroids of the two beams in the transverse plane, σ_{kl} the beam size of beam k and plane l and $\mathcal{L}_0$ the targeted luminosity for each experiment $\mathcal{L}_0$ [11]. Within this approximation we overlook that the bunches have been deformed due to the effect of the crab cavity modulation [12] as well as other effects that contribute to the luminosity loss such as the hourglass effect [13]. Indeed, the luminosity loss factor is overestimated by up to 10% using Eq. 11 with respect to the luminosity loss factor calculated taking into account all these effects. In Tab. 1 the luminosity loss factor due to the orbit effects of the beam-beam interactions are summarized for the two high luminosity experiments and the nominal and ultimate scenarios during collision. The calculation has been done using the code PyLumi [14] that allows to compute the luminosity of two crossing bunches taking into account the effect of an offset between them, the crossing angle and the crab cavity modulation as well as the hourglass effect. The values reported in Tab. 1 correspond to the luminosity loss originated by the PACMAN beam-beam effects $\frac{\Delta\mathcal{L}}{\mathcal{L}_0}$, where $\mathcal{L}_0 = 5.33\cdot 10^{34}$ cm^{-2}s^{-1} and $\mathcal{L}_0 = 7.80\cdot 10^{34}$ cm^{-2}s^{-1} are the integrated luminosity for the nominal and ultimate scenarios once the effect of the crossing angle, the crab cavity modulation and the hourglass effect have been taken into account. We note that the estimations of the peak luminosity exceed the design, as the residual crossing angle due to the limited strength of the crab cavities was neglected. This approximation does not impact the accuracy of the luminosity loss factor significantly. The targeted luminosity of each experiment can be found in [11].

3.1.2 IMPACT ON THE REQUIRED PHYSICAL APERTURE

We focus on the most critical configuration, i.e. at the start of collision in the ultimate scenario (Fig. 7). It is expected that the effect of the orbit spread on the required physical aperture is most critical inside the triplets where the β function is large. As discussed later, the largest spread is found inside the left

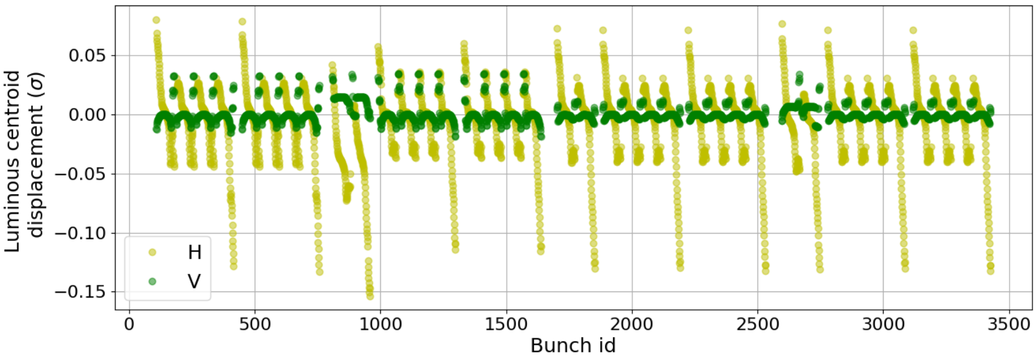

(a) IP1 (Atlas).

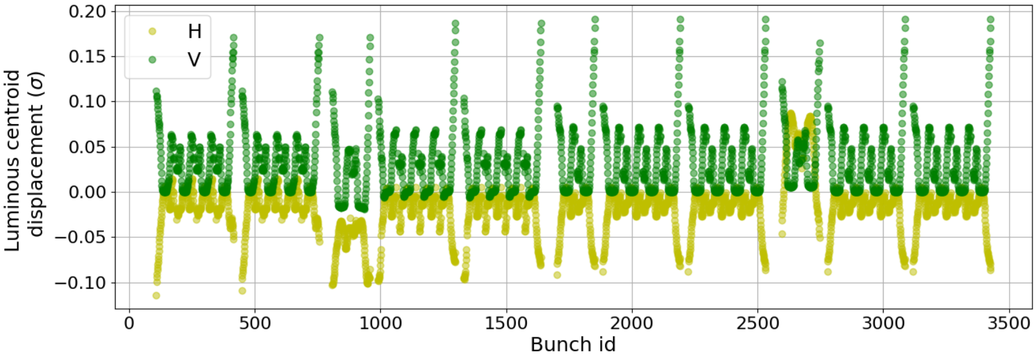

(b) IP2 (Alice).

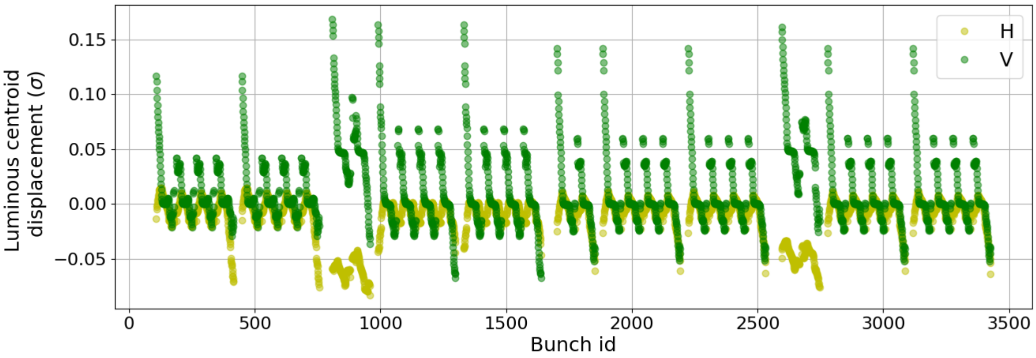

(c) IP5 (CMS).

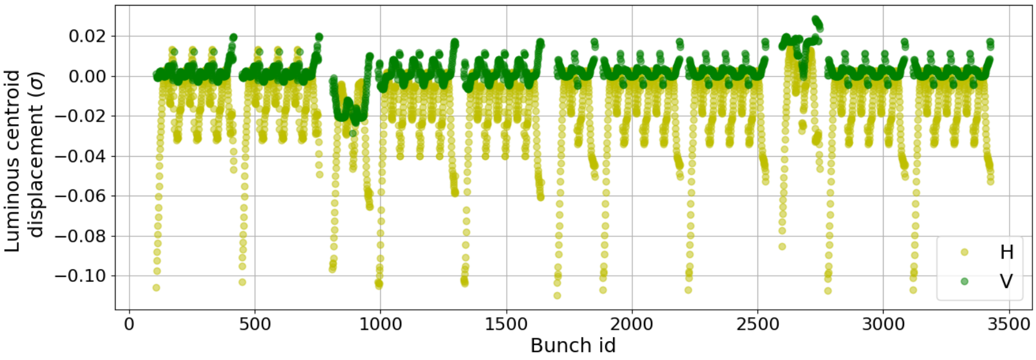

(d) IP8 (LHCb).

Figure 8: Luminous centroid displacement in the four IPs for the nominal scenario in collision using the standard filling scheme.

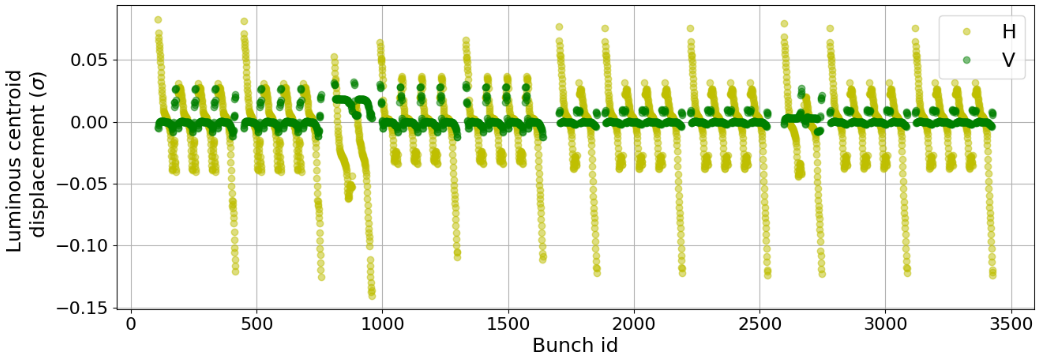

(a) IP1 (Atlas).

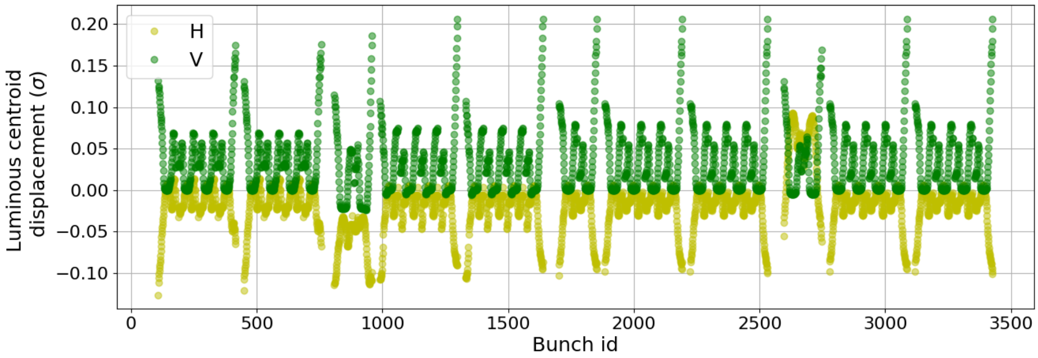

(b) IP2 (Alice).

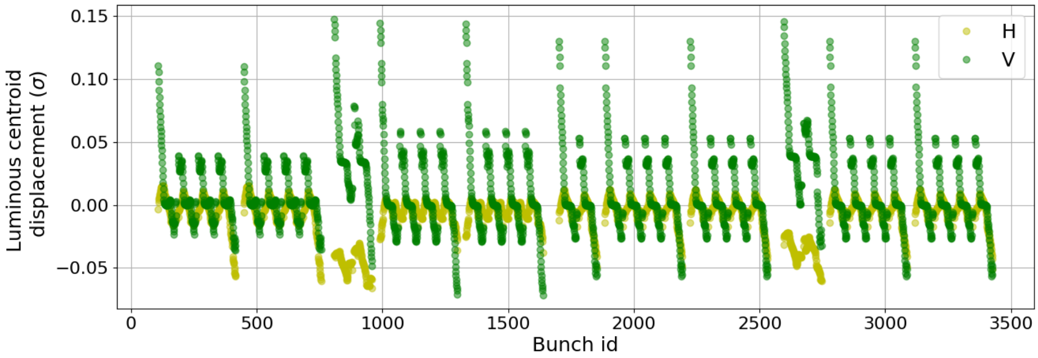

(c) IP5 (CMS).

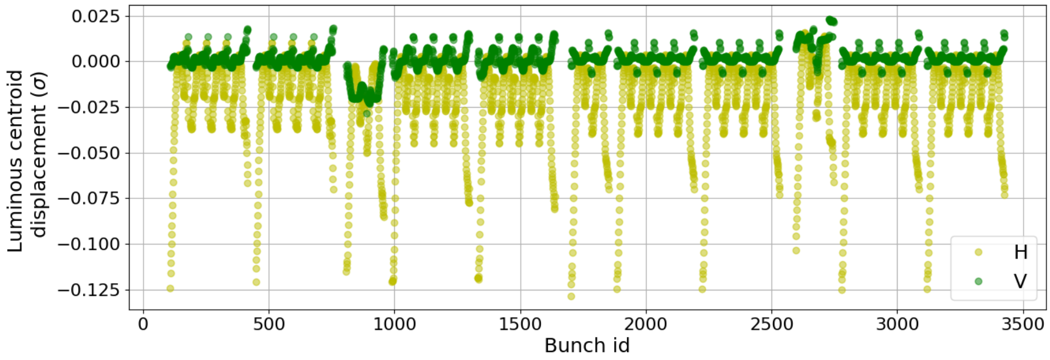

(d) IP8 (LHCb).

Figure 9: Luminous centroid displacement in the four IPs for the ultimate scenario in collision using the standard filling scheme [3].

	Nominal scenario	**Ultimate scenario**
IP1	0.11	0.16
IP5	0.08	0.10

Table 1: Luminosity loss factor $\frac{\Delta\mathcal{L}}{\mathcal{L}_0}$ in % due to PACMAN effects for the high luminosity experiments for the nominal and ultimate scenarios respectively.

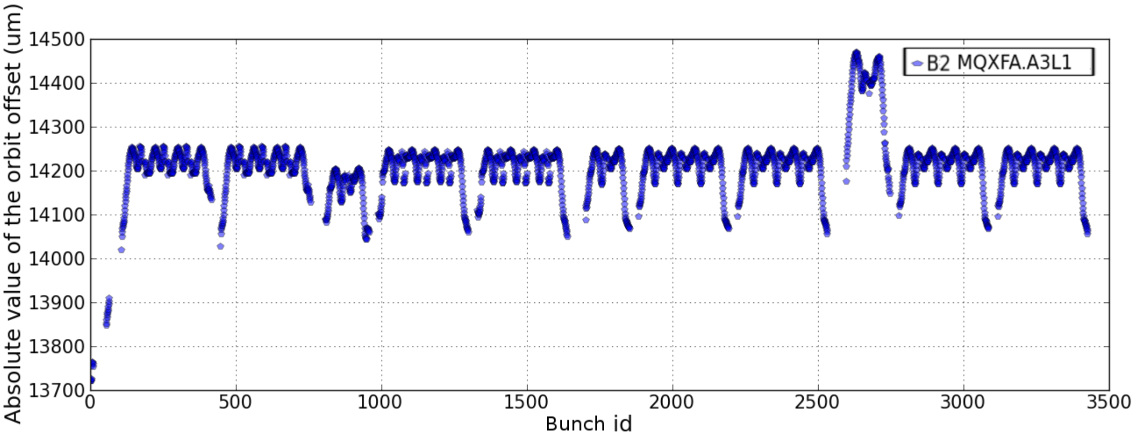

Figure 10: Orbit offset in micrometers as a function of the bunch ID for the horizontal plane of beam 2 at the start of collision for the ultimate scenario (β^* of 41 cm) in the triplet at the left of IP1 and using the standard filling scheme.

triplets of IP1 for beam 2, the orbit of individual bunches at this location is shown in Fig. 10. The spread due to long-range interactions at IP1 (M shape visible for all bunch trains) corresponds approximatively to 0.1 σ. The 2 short trains (12 bunches at the beginning of the beam) miss significantly more long-range interactions in IPs 1 and 5 resulting in a larger shift of about 0.55 mm with respect to the nominal bunches, i.e. those experiencing all beam-beam interactions. This corresponds to about 0.4 σ at that location. The bunches located at slots 2590 to 2770 exhibit also a large orbit shift ($\approx 0.15\sigma$) with respect to the nominal bunches due to the missing offset interaction at IP2, yielding a full peak-to-peak orbit spread above half the beam size.

Although the largest orbit shift affects a relatively small set of bunches, their orbits remain relevant when considering the asynchronous beam dump. In this failure scenario, the kickers are fired out of synchronization with the abort gap. Even though the 15 kickers are fully synchronized, the bunches that pass through the kickers during their rise of the voltage will experience an oscillatory trajectory with a large amplitude and therefore could impact and damage sensitive elements of the accelerator [15, 16]. The rise time of the dump kickers could deviate approximately 8 consecutive bunches, thus the orbit of the super-PACMAN bunches of IPs 2 and 8, as well as the short 12 bunch trains must be taken into account.

We therefore need to establish a robust criterion for the effect of PACMAN bunches on the required aperture. We sum up the contributions from missing beam-beam interactions for the different sets of bunches, assuming pessimistically that the phase advances of the different sources are such that they add up at the aperture bottlenecks. The resulting orbit shift for various combinations of PACMAN and super-PACMAN effects are shown in Tab. 2. We note that some combination of missing interactions do not exist in the nominal filling pattern, such as bunches missing interactions in all IPs. They may exist for short periods of the run when the machine is operated with special filling schemes used for example during validation phases such as the intensity ramp up. Setting aside those special configurations, the maximum orbit shift may reach 0.44 σ.

The potentially most critical set of bunches correspond to those missing long-range interactions on one side of IPs 1 and 5 and all interactions in IP8, quoted IP15 PACMAN+IP8 super-PACMAN in the Tab 2.

Nick name	IPs 1 and 5		IP2		IP8		Max. tot.
	HO	LR	HO	LR	HO	LR	[σ]
IP15 PACMAN	0	0.22	0	0	0	0	0.22
+IP2 PACMAN	0	0.22	0	0.05	0	0	0.27
+IP8 PACMAN	0	0.22	0	0	0	0.06	0.26
+IP2 super-PACMAN	0	0.22	0.1	0.1	0	0	0.43
+IP8 super-PACMAN	0	0.22	0	0	0.1	0.12	0.44
IP15 super-PACMAN	0	0.43	0	0	0	0	0.43
+IP2 PACMAN	0	0.43	0	0.05	0	0	0.48
+IP8 PACMAN	0	0.43	0	0	0	0.06	0.49
+IP2 super-PACMAN	0	0.43	0.1	0.1	0	0	0.63
+IP8 super-PACMAN	0	0.43	0	0	0.1	0.12	0.65

Table 2: Summary of the maximum orbit shift with respect to the nominal bunch, i.e. to the bunch experiencing all beam-beam interactions, to bunches missing interactions in different locations. The PACMAN bunches miss all long-range interactions on one side of the given IP, whereas super-PACMAN miss all long-range interactions as well as the head-on interaction. All values are provided for the ultimate scenario at the start of collision with $\beta^* = 41$ cm and a normalised emittance of 2.5 μm. The total assumes the worst phase advance between the sources such that their contributions add up. The contribution from the offset interaction at the IPs 2 and 8 is assumed at the maximum of the beam-beam force (Eq. 1). The highlighted rows represent bunches that do not exist in the nominal filling pattern, however they could exist with others, such as those used during the intensity ramp up.

The contribution from IPs 1 and 5 remains about constant through the luminosity levelling with β^* as the reduction of the strength of long-range interactions due to the decaying bunch intensity is compensated by the reduction of β^*. On the other hand the contributions of long-range interactions in IP8 as well as the offset collision at the IP only reduced during the fill. The second most critical contribution, i.e. the bunches missing all beam-beam interactions in IPs 1 and 5 is expected to remain constant through the fill for the same reason discussed. Thus this contribution prevents a reduction of the physical aperture requirement due to PACMAN orbit effects throughout the fill.

Based on the considerations above we find that the protected aperture should be adjusted to take into account a potential orbit shift up to 0.44 σ of tens of consecutive bunches. Similar considerations at injection energy lead to a maximum shift of 0.6σ 3. This additional margin may be reduced if needed by considering, and possibly optimising, the phase advances between the IPs and the sensitive aperture bottlenecks [15].

3.1.3 CRAB CAVITY LOADING

The crab cavities are installed around IPs 1 and 5 to compensate partly the geometric reduction of luminosity due to the beam crossing angle at the IP. Since these are cavities generating transverse fields, a variation of the beam offset in the cavity will result in an induced voltage. Since former versions of TRAIN were limited to the estimation of the orbit effect at the location of beam-beam interactions, a coarse extrapolation of the orbit effect at the crab cavities was used to estimate the induced voltage yielding approximately 2 kV, i.e. less than 0.1% of the nominal cavity voltage 3.4 MV for an horizontal orbit spread of $\approx$ 360 μm at the crab cavities [12]. TRAIN was extended to allow for an accurate estimation of bunch-by-bunch orbit at any location [8], confirming the validity of the extrapolation, with orbit spreads ranging from 100 μm to 500 μm, as it can be seen in Fig. 11.

Nick name	IPs 1 and 5		IP2		IP8		Max. tot.
	HO	LR	HO	LR	HO	LR	$[\sigma]$
IP15 PACMAN	0	0.19	0	0	0	0	0.19
+IP2 PACMAN	0	0.19	0	0.21	0	0	0.40
+IP8 PACMAN	0	0.19	0	0	0	0.21	0.41
+IP2 super-PACMAN	0	0.19	0	0.41	0	0	0.60
+IP8 super-PACMAN	0	0.19	0	0	0	0.41	0.60
IP15 super-PACMAN	0	0.38	0	0	0	0	0.38
+IP2 PACMAN	0	0.38	0	0.21	0	0	0.59
+IP8 PACMAN	0	0.38	0	0	0	0.21	0.59
+IP2 super-PACMAN	0	0.38	0	0.41	0	0	0.79
+IP8 super-PACMAN	0	0.38	0	0	0.0	0.41	0.79

Table 3: Summary of the maximum orbit shift with respect to the nominal bunch, i.e. to the bunch experiencing all beam-beam interactions, to bunches missing interactions in different locations. The PACMAN bunches miss all long-range interactions on one side of the given IP, whereas super-PACMAN miss all long-range interactions as well as the head-on interaction. All values are provided for the ultimate scenario at injection with $\beta^* = 6$ m and a normalised emittance of 2.5 μm. The total assumes the worst phase advance between the sources such that their contributions add up. The contribution from the offset interaction at the IPs 2 and 8 is assumed at the maximum of the beam-beam force (Eq. 1). The highlighted rows represent bunches that do not exist in the nominal filling pattern, however they could exist with others, such as those used during the intensity ramp up.

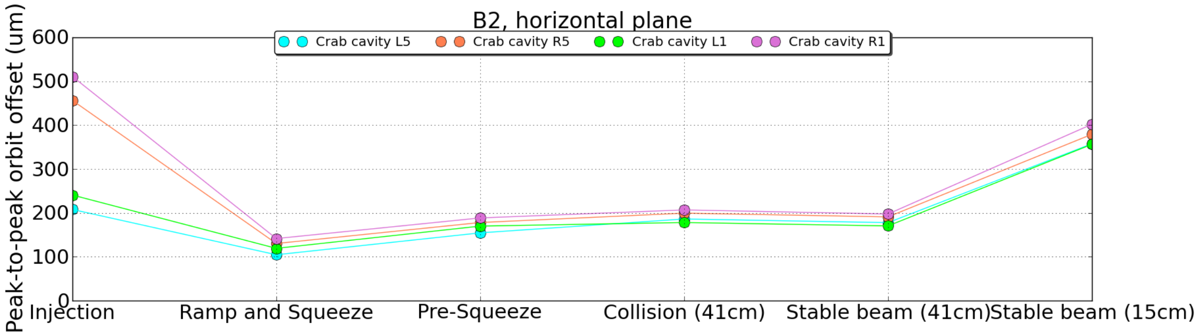

Figure 11: Maximum peak-to-peak orbit spread for the horizontal plane of beam 2 at the crab cavities located at the right and left of IP5 and IP1.

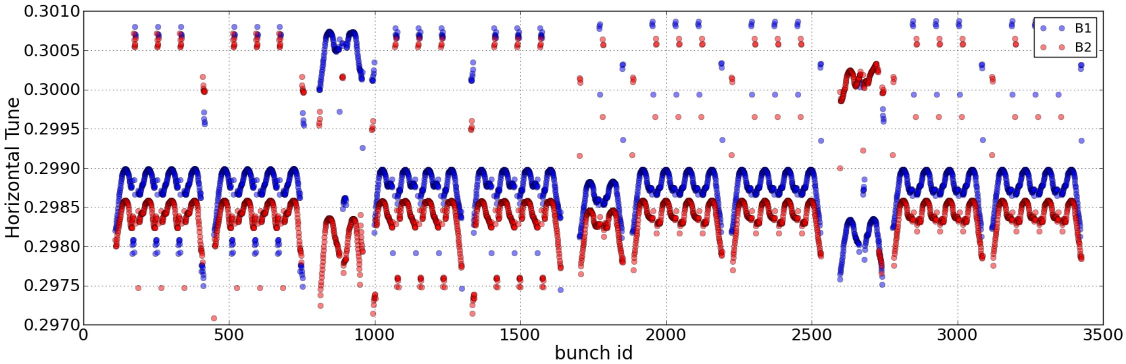

(a) Horizontal tune.

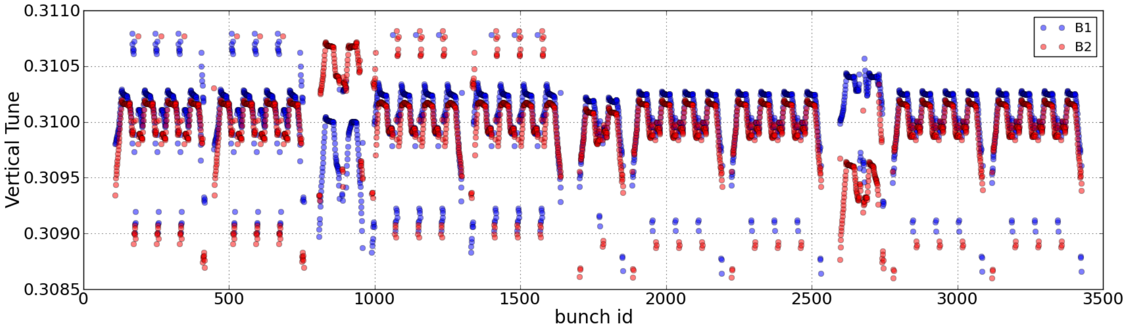

(b) Vertical tune.

Figure 12: Tune as a function of the slot number for beam 1 and 2 for the nominal scenario with collision optics. The outstanding bunches are experiencing either super-PACMAN encounters at IP2 or IP8. The sets of bunches 800 to 990 and from 2590 to 2770 are missing interactions at IPs 2 and 8.

3.2 Tune effects

The beam-beam interactions also produce a change on the tunes of both beams that can be globally corrected so that the dynamic aperture is not compromised. However, the PACMAN effects derived from the beam-beam interactions will also produce bunch-by-bunch differences on the tunes that may challenge such a correction. Therefore, the effect of the beam-beam PACMAN interaction on the dynamic aperture must be taken into consideration.

As it was detailed in [17], the tune change produced by a head-on beam-beam interaction without crossing angle driven by round beams is given by

$$\Delta Q_{HO} = -\frac{N r_p}{4\pi\varepsilon} \tag{12}$$

in both planes and the tune shift due to the long-range interactions on one side of a single IP, i.e. without compensation between IPs 1 and 5, can be approximated by

$$\Delta Q_{LR} = \pm N_{LR} \frac{N r_p}{2\pi\varepsilon d^2} \tag{13}$$

which achieves values up to 1.2 $\times 10^{-3}$ for the ultimate scenario. TRAIN provides the tune per bunch, showing patterns such as Fig. 12 for the standard filling scheme during collision with all 4 IPs, that match the order of magnitude predicted by Eqs. 12 and 13.

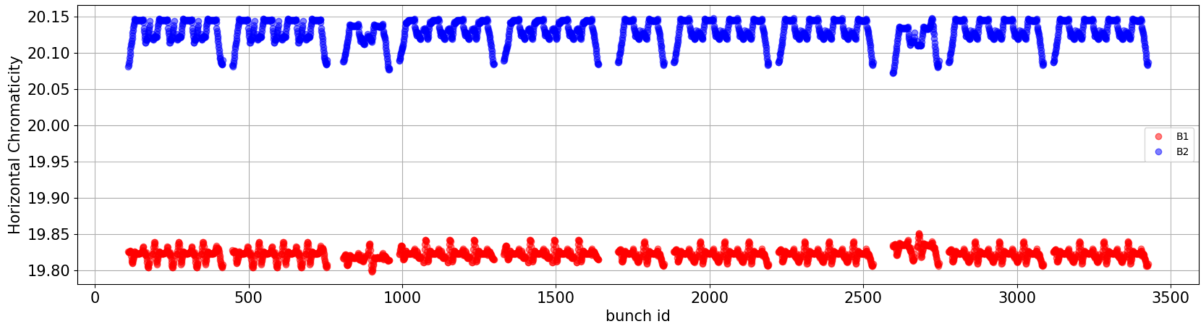

(a) End of ramp and squeeze. (Q'_0=20)

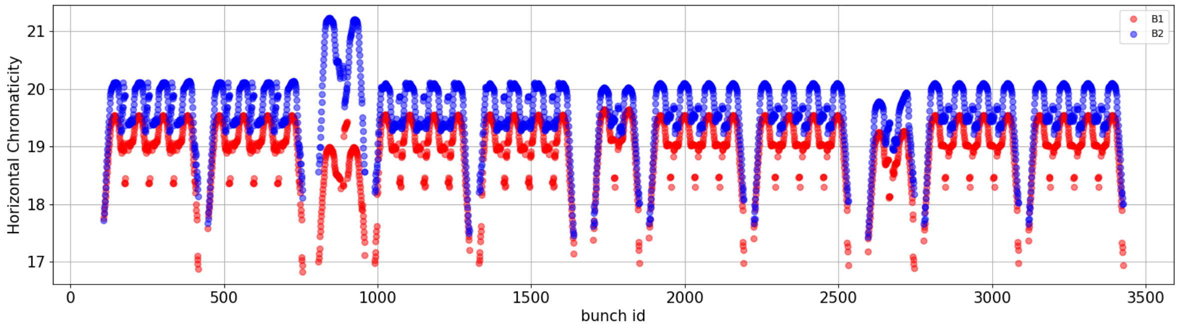

(b) Start of collision (Nominal scenario, $\beta^* = 64$ cm, Q'_0=15).

Figure 13: Horizontal chromaticity for beam 1 and 2 during the end of ramp and squeeze and the start of collision for the nominal scenario. The unperturbed chromaticity is labelled as Q'_0. The standard filling scheme has been used. A similar behaviour is observed in the vertical plane.

3.2.1 IMPACT ON THE DYNAMIC APERTURE

The dynamic aperture is highly dependent on the choice of working point and, in absence of bunch-by-bunch tune control, the uncompensated (super-)PACMAN tune shifts results in a spread of working points in the order of 2×10^{-3} in the horizontal tune and of 1.2×10^{-3} for the vertical one, as shown in Fig 12. Fortunately, the (super-)PACMAN bunches also experience less non-linearities w.r.t. nominal bunches and therefore their tolerance for tune shifts is relaxed. Numerical studies based a configuration similar to the ultimate scenario at the start of collision, but with a normalised separation between the beams increased by 20% shows a tolerance on the tunes of $5 \cdot 10^{-3}$ to maintain the dynamic aperture above 6 σ [19] which seem sufficient to account for the PACMAN tune shifts in this relaxed configuration. Nevertheless the margins are tight, suggesting that detailed dynamic aperture simulations have to be performed also for PACMAN bunches in the present ultimate scenario in which long-range interactions are about 20% stronger. Other effects with a potential impact on the dynamic aperture of PACMAN bunches are discussed below.

3.3 Chromaticity effects

The chromaticity spread is a major concern for the beam stability, which is most critical before collision. It can also reduce the beam lifetime during collision, so we will concentrate on the analysis of the chromaticity at these stages of the operation cycle. As for other PACMAN effects, the chromaticity spread is more of a concern than the shifts as the latter can be corrected globally during operation. Nevertheless, we note that no online measurement of the chromaticity are currently foreseen. Instead the empirical measurement measurement and correction of the chromaticity will have to be performed using an en-

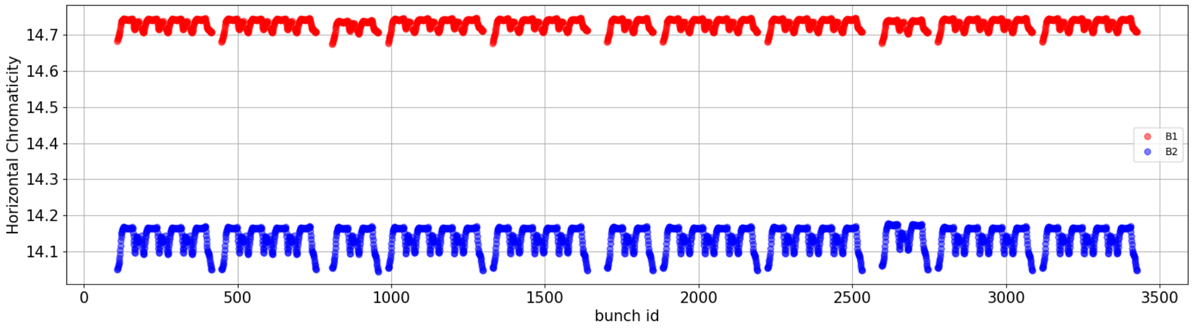

(a) End of the pre-squeeze process. (Q'_0=15)

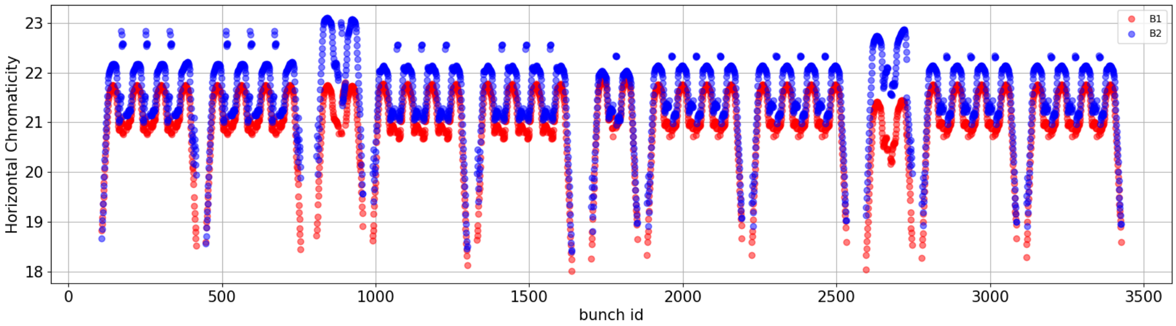

(b) Start of collision (Ultimate scenario, $\beta^* = 41$ cm, Q'_0=15).

Figure 14: Horizontal chromaticity for beam 1 and 2 at the end of the pre-squeeze and the start of collision for the ultimate scenario. The unperturbed chromaticity Q'_0 is 15 units. The standard filling scheme has been used. A similar behaviour is observed in the vertical plane.

ergy modulation on a low intensity beam which does not feature all of these effect. Consequently, their corrections would need to performed based on the model.

In the following we identify the two main sources of chromaticity shift and spread before and during collisions to be respectively the β-beating at the lattice sextupoles due to the quadrupolar component of the long-range force before collision and an interplay of the orbit effect driven by long-range interactions in the presence of an uncorrected dispersion at the IP once in collision. In Figs. 13 and 14, the horizontal chromaticity at the end of ramp and squeeze, at the end of the pre-squeeze and at the beginning of collision for the nominal and ultimate scenarios are shown. It can be appreciated that the chromaticity shift and spread before collision remains in the order of a unit or less in both the nominal and ultimate scenario (Figs. 13a and 14a), while once in collision the shift and the spread of chromaticity can exceeds 5 units (Figs. 13b and 14b).

Before collision the chromaticity spreads and shifts are compatible with a modification of the chromaticity correction with lattice sextupoles due to the optics distortions produced by beam-beam interactions. Indeed, an upper bound of the shift can be estimated considering the quadrupolar component of the beam-beam interaction, we can write the maximum β-beating corresponding to a given tune shift [9]

$$\max \frac{\Delta\beta}{\beta} = \frac{2\pi\Delta Q_{LR}}{\sin(2\pi Q)} \tag{14}$$

with ΔQ_{LR}, the tune shift due to the long-range interactions (Eq. 13). Since the correction is proportional to the β function, we can estimate an upper bound of the variation of chromaticity corresponding to the least favourable phase advance between the beam-beam interactions and the lattice sextupoles [9]

$$|\Delta Q'| < \|(Q' - Q'_{nat})\frac{\Delta\beta}{\beta}\| \tag{15}$$

with a natural chromaticity of $Q'_{nat} \approx -150$ units. For instance, at the end of ramp and squeeze, the estimated chromaticity spread Eq. 15 that we obtain with the estimated β-beating computed as Eq. 14 is up to 1.6 units for the nominal scenario and 3 for the ultimate one.

These estimates are compatible with the requirements to control chromaticity within 2 units to avoid coherent instabilities [24].

Although the effect of beam-beam induced β-beating on the chromaticity correction scheme matches the order of magnitude of the chromaticity shift and spread before collision, it is not sufficient to the amplitude of the effect observed in collision suggesting that another contribution arise from the head-on interaction at the IPs. On the other hand, the variation of the chromaticity shift for the bunches at the head and the tail of the trains indicates that this contribution is also affected by long-range interactions. This combined effect of long-range and head-on interactions can be understood as the chromaticity shift and spread generated by a slightly offset collision at the IP caused by the long-range interactions together with an uncorrected dispersion of few millimeters at the IP, that can be expected due to the imperfect correction of the dispersion at the IP [20]. For small offsets this contribution is given by [21]

$$\Delta Q' \approx \frac{2\Delta Q_{HO}}{7d^3}\eta^* \tag{16}$$

where η^* is the dispersion at the IP normalised by the beam size, d is the normalised separation at the IP and ΔQ_{HO} refers to Eq. 12. Using Eq. 16 for a dispersion of 1 mm and a separation at the IP of 0.1 σ we obtain a chromaticity shift up to 40 units.

We note that TRAIN does not allow for a re-optimisation of the orbit once beam-beam effects are taken into account. In practice, the orbit will be readjusted such that the nominal bunches are exactly head-on, since this configuration maximises the luminosity. Being proportional to the offset at the IP, the chromaticity shift is expected to vanish for the nominal bunches. On the other hand, the spread of approximatively 3 units is expected to remain for PACMAN bunches.

Dynamic aperture calculations for colliding beams suggest that a chromaticity shift of 5 units can be acceptable, depending on the configuration and in particular the octupole current [22]. We note two aspects related to the handling of this large chromaticity shift in collision. First, the role of the octupoles for keeping the beam stability is reduced, since the large Landau damping generated by head-on beam-beam interactions is sufficient to maintain the beam stability independently of the octupole current. Therefore an optimisation is possible to account for the chromaticity shifts expected. Second, it is expected that this effect reduces significantly for particles oscillating with a large amplitudes in the transverse plane, as the head-on beam-beam force vanishes. This strong chromo-geometric aberration has a different impact on the dynamic aperture w.r.t. chromaticity, therefore the direct comparison with simulations in [22] is only indicative. In particular, a correction of the linear chromaticity with the arc sextupoles might not be optimal, since the chromaticity shift of particles in the transverse tails, i.e. oscillation with a large transverse amplitude, differs significantly from the particles in the core of the beam distribution.

3.3.1 THE EFFECTS OF THE ARC OCTUPOLES AND THE DISPERSION CORRECTION SCHEME

PACMAN chromaticity is also generated indirectly by the arc octupoles, due to the beam offset at their location generated by the beam-beam interactions. Through feed-down effect this results effectively in a sextupolar component in a dispersive area and consequently chromaticity. As the feed-down is different for every bunch, so is the generated chromaticity. This contribution was estimated at all stages of the cycle, for both the nominal and ultimate scenarios by comparing the chromaticity spread with the octupoles turned on or off, yielding a difference below 0.01 units of chromaticity. The amplitude of this effect is expected to vary due to the implementation in the HL-LHC of a correction scheme for the dispersion generated by the crossing angle involving a variation of the dispersion in the arc [23], i.e. at the location of the octupoles. In addition, as a direct result of the correction of the dispersion in the interaction region, the contribution of long-range interactions to chromaticity via their sextupolar component is reduced. In all configurations these effect remain small, as illustrated by Fig. 15. Indeed, at the end of the combined ramp and squeeze during which there are only long-range interactions between the beams (Fig. 15a), the spread is almost identical in all configurations of octupole and dispersion correction. In collision (Fig. 15b), there is a large difference in spread between the configurations with and without dispersion correction, due to effect of the residual dispersion at the IP discussed above (Eq. 16), however the contribution of the octupoles to the chromaticity spread is small in both cases.

While the effect on the spread is small, Fig. 15 exhibits large chromaticity shifts with respect to the nominal values of chromaticity when the octupoles are activated or desactivated and the crossing angle dispersion correction scheme enabled or disabled. Without the dispersion correction the presence of the octupoles induce a chomaticity shift change of magnitude ≈ 0.02 units in all the phases of the operational cycle, but when the dispersion correction is applied the chromaticity shift change is up to ≈ 0.8 units. This shift in chromaticity comes from the quadrupolar component of the field in the lattice octupoles, since it is a consequence of a tune shift of magnitude $\Delta(\Delta Q) \approx 0.0018$ units between the case with dispersion correction and dispersion correction plus active octupoles, as it can be seen in Fig. 16, where the change in tune due to the presence of the octupoles has been represented. Evaluating the change in chromaticity expected due to the β-beating at the lattice sextupoles, using Eqs. 14 and 15 due to the change in tune of 0.0018 units, we obtain an upper bound to the change in chromaticity of approximately 2 units for the case of the nominal scenario with collision optics and 2.9 units of chromaticity for the ultimate scenario. Therefore, the order of magnitude of the maximum shift in chromaticity due to the quadrupolar feed-down in the lattice octupoles is consistent with the shift in

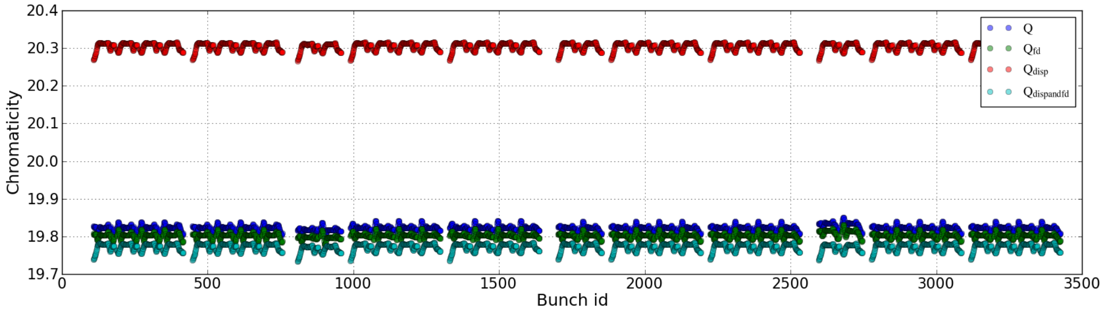

(a) End of the ramp and squeeze ($Q'_0 = 20$).

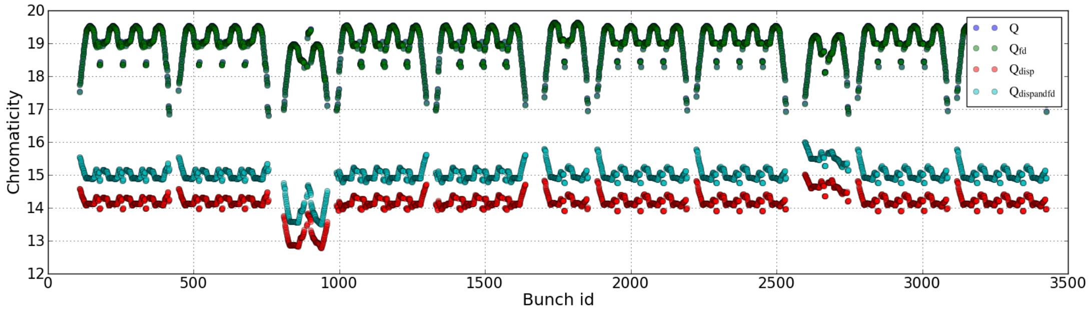

(b) Start of collision (Nominal scenario, $\beta^* = 64$ cm, $Q'_0 = 15$).

Figure 15: Horizontal chromaticity for beam 1 at the end of the combined ramp and squeeze and at the start of the collision for the nominal scenario. The results without crossing angle dispersion correction scheme with the octupoles turned off and on are represented by blue and green dots respectively. Similarly the results with the dispersion correction enabled are represented by red and cyan dots. The standard filling scheme has been used.

chromaticity that we observe in Fig. 15. This correction in chromaticity comes from the properties of the dispersion correction, but it is not influenced by the PACMAN effects since, as we have discussed the chromaticity spread is barely affected.

3.4 Linear coupling

The strength of the coupling resonance $|C^-|$ is usually quantified by the closest tune approach of the coupled system, with the tune separation defined as $\Delta Q = |Q_u - Q_v|$ with Q_u and Q_v the coupled tunes. The linear coupling is generated by the beam-beam interaction with a transverse offset in both transverse planes and its effect may be specially relevant before the establishment of the head-on interaction, since it is one of the causes of the loss of Landau damping generated by the octupoles [25]. In particular, during the end of the ramp and the squeeze for both the nominal and ultimate operational cycles, the combination of the parallel separation and crossing angle bumps generate long-range interactions on a skew plane, generating potentially a closest-tune-approach of $|C^-| \approx 2.5 \cdot 10^{-4}$ per IR side and a bunch coupling spread of the same order of magnitude. The effect of the separation bump does not represent an issue for beam instability as the tolerance for linear coupling is set at 10^{-3} when operating with a tune separation of $5 \cdot 10^{-3}$ [33]. However, in recent experiments [26] a long-range generated linear coupling of 10 times this expected value was observed and is, consequently, above the tolerance. In the following we develop the tools required to investigate the source of this difference.

Following [17], an analytical expression for the coupling strength resulting from the quadrupolar

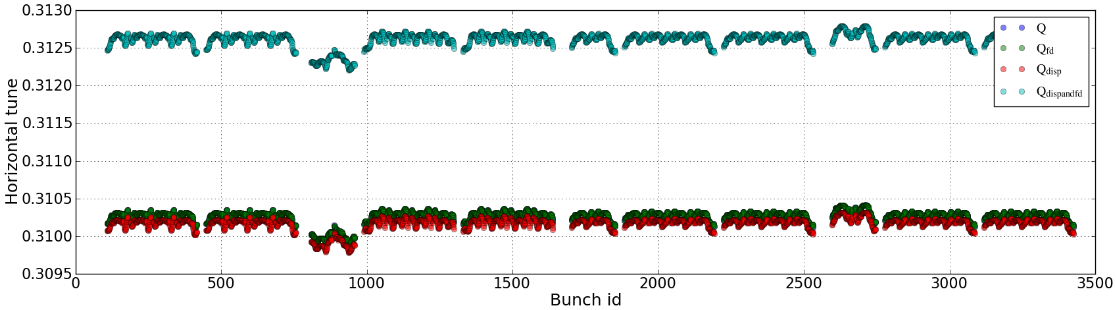

(a) End of ramp and squeeze ($Q_0 = 0.31$).

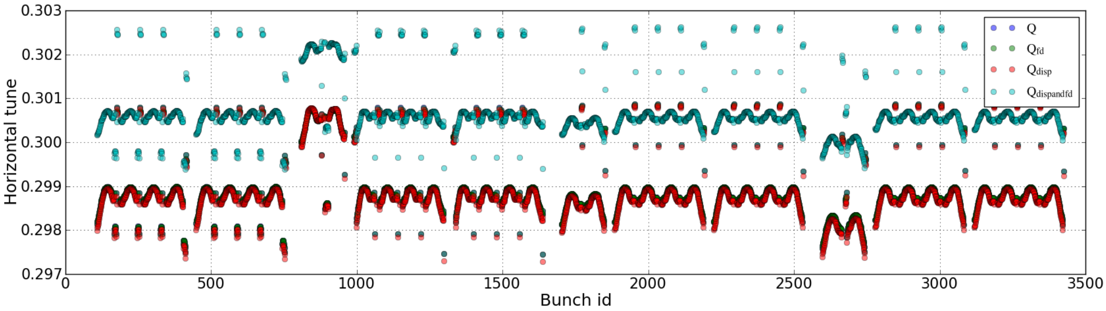

(b) Start of collision (Nominal scenario, $\beta^* = 64$ cm, $Q_0 = 0.31$).

Figure 16: Horizontal tune for beam 1 at the end of the combined ramp and squeeze and at the start of the collision for the nominal scenario. The results without crossing angle dispersion correction scheme with the octupoles turned off and on are represented by blue and green dotes respectively. Similarly the results with the dispersion correction enabled are represented by red and cyan dots. The standard filling scheme has been used.

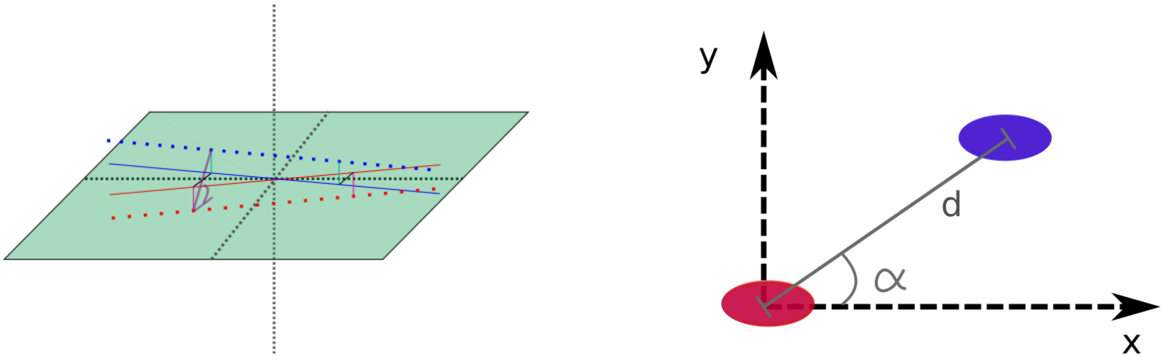

(a) (b)

Figure 17: Representation of a long-range collision with a skewed offset d of angle α in the x-y plane.

component of the long-range interaction can be derived from the beam-beam kick imposing:

$$\frac{\partial \Delta x'}{\partial y}(x = d\cos(\alpha), y = d\sin(\alpha)) = \frac{\partial \Delta y'}{\partial x}(x = d\cos(\alpha), y = d\sin(\alpha)) \tag{17}$$

since the presence of a long-range collision with an inclined offset behaves as a skew quadrupole at the location of the long-range interaction. Adding all the one-side contributions of all long-range interactions we reach the expression derived in [17, 27]

$$k = 2\frac{r_p N}{\pi \varepsilon} \sum_{i}^{N_{LR}} \frac{\sin(\alpha_i)\cos(\alpha_i)}{d_i^2} \tag{18}$$

where α is the roll angle of the interaction with respect to the horizontal plane, as schematically represented in Fig. 17, and d is the normalised distance between both beams. This approximation holds for long-range interactions, so, for d $< 4\sigma$ it is expected to present discrepancies with respect to $|C^{-}|$. Also, it is important to highlight that this model accounts just for a single IP and does not allow to predict the effect of long-range interactions taking place in another IP. The linear coupling $|C^{-}|$ can also be calculated directly from the one-turn map, including the effect of the beam-beam interactions in a single or several IPs, thus avoiding the approximations that we did while deriving Eq. 18 and the restriction of the single IP. Furthermore, using the one-turn maps including the beam-beam interactions the Twiss parameters in the presence of coupling can also be obtained.

3.4.1 Derivation of the coupled Twiss parameters and $|C^{-}|$

Following [28], an initial 4×4 symplectic matrix M can be divided into 4 block 2×2 matrices

$$M = \begin{pmatrix} A & B \\ C & D \end{pmatrix}, \tag{19}$$

so the normal form of the input matrix $M_{\perp}$ (block diagonal) can be found defining a similarity R_M such that transforms M into $M_{\perp}$

$$M_{\perp} = g^2 \bar{R}_M M R_M = \begin{pmatrix} E & 0 \\ 0 & F \end{pmatrix}. \tag{20}$$

The similarity transformation is defined as in [29]

$$R_M = \begin{pmatrix} \mathbb{I} & \bar{R} \\ -R & \mathbb{I} \end{pmatrix}, \tag{21}$$

and the transformation factor g satisfies the relationship $g^2 \bar{R}_M R_M = \mathbb{I} \rightarrow g = |R_M|^{-\frac{1}{2}}$.

In Eq. 21, the bar refers to the symplectic conjugate of the given matrix, which is defined as:

$$\bar{R} = -SR^T S, \quad S = \begin{pmatrix} S_2 & & \\ & S_2 & \\ & & \ddots \end{pmatrix} \tag{22}$$

being $S_2 = \begin{pmatrix} 0 & 1 \\ -1 & 0 \end{pmatrix}$ the 2×2 symplectic matrix.

The block similarity R can be found to be [29]

$$R = -(\frac{1}{2}(\mathrm{Tr}A - \mathrm{Tr}D) + \frac{1}{2} sign(\mathrm{Tr}A - \mathrm{Tr}D)\sqrt{\Delta})^{-1}(C + \bar{B}) \tag{23}$$

with $\Delta = (\mathrm{Tr}A + \mathrm{Tr}D)^2 + 4|C + \bar{B}|, \quad g = (1 + |R|)^{-\frac{1}{2}}$. Once the transformation has been found the block diagonal matrices E and F can be found applying the transformation described in Eq. 20, or simply

$$E = A - BR \tag{24}$$

$$F = D + RB \tag{25}$$

Once the one-turn map has been converted to normal form, the Twiss parameters in presence of coupling can be extracted using the standard formulas [30]

$$m_{\perp,i} = \begin{pmatrix} \cos\theta_i + \alpha_i \sin\theta_i & \beta_i \sin\theta_i \\ -\gamma_i \sin\theta_i & \cos\theta_i - \alpha_i \sin\theta_i \end{pmatrix} = \begin{pmatrix} m_{i,1,1} & m_{i,1,2} \\ m_{i,2,1} & m_{i,2,2} \end{pmatrix} \tag{26}$$

where $m_{\perp,i}$ is the upper or lower 2×2 block diagonal matrix obtained from the block diagonalization of Edward and Teng. The value of the α and β functions at the IP where the calculation is being done can be obtained. The eigentunes $\theta_i = 2\pi Q_i$ can be directly obtained from Eq. 26,

$$\cos\theta_i = \frac{1}{2}\mathrm{Tr}(m_{\perp,i}), \quad \cos\theta_i = \mathrm{sign}(m_{i,1,2})\sqrt{-m_{i,1,2}m_{i,2,1} - \left(\frac{1}{2}\mathrm{Tr}(m_{\perp,i})\right)^2} \tag{27}$$

and will allow to compute the tunes of both modes e and f in the presence of coupling.

The closest tune approach can be computed using the obtained coupled tunes as follows [28]

$$|C^-| = \frac{\sqrt{|C + \bar{B}|}}{\pi(\sin\theta_e + \sin\theta_f)} \tag{28}$$

with $|C + \bar{B}|$ denoting the determinant of the sum of the off diagonal 2×2 off-diagonal block matrices the one-turn map (Eq. 19) and $\theta_e = 2\pi Q_e$ and $\theta_f = 2\pi Q_f$, with Q_e and Q_f the coupled tunes.

The closest tune approach computed using Eq. 28 and implemented within TRAIN has been benchmarked against the analytical formula Eq. 18 derived in [17, 27] using the presence of a randomly introduced skew quadrupole in the lattice with a tilting of 45° and without beam-beam interactions for a single long-range interaction at IP5. In Fig. 18 both methods are compared in logarithmic scale as a function of the distance during collision. As it can be observed, the agreements worsens for small normalised distances, approximately for $d << 5\sigma$, as expected due to the approximations that we did while deriving Eq. 18. It is also interesting to notice that as an advantage with respect to Eq. 18, Eq. 28 has been derived from the one-turn maps including beam-beam interactions, and thus allows to estimate the linear coupling in the presence of beam-beam interactions at several IPs. As we will see in Figs. 20 and 23, we obtain with TRAIN an estimation of the linear coupling of the order of 10^{-3} in the presence of beam-beam interactions in two IPs with perpendicular crossing angle planes, due to the induced orbit offsets introduced by the beam-beam interactions. This prediction is around a factor 2 smaller than the measurements reported in [26], rather than the factor 10 that we obtained using the analytical approach Eq. 18, that overlooks the effect of the offsets generated in other IPs.

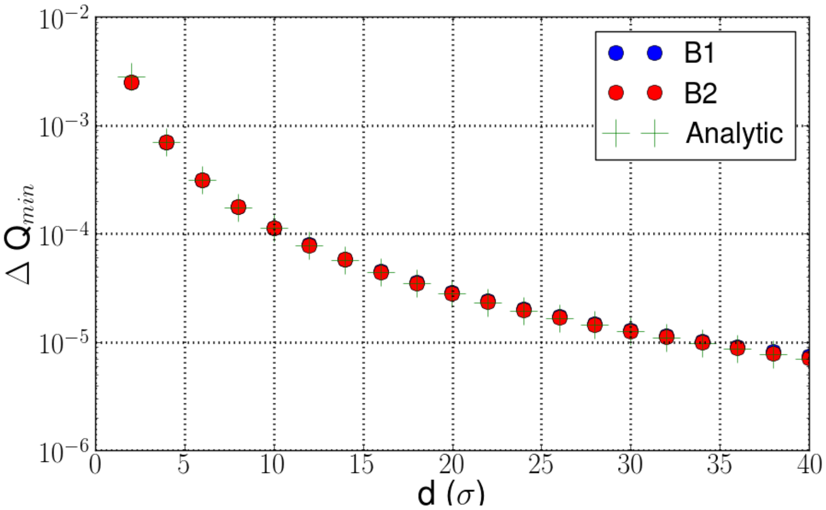

Figure 18: Benchmark of $|\Delta Q|_{min}$ obtained with TRAIN using the implementation of Eq. 28 for a configuration with a single beam-beam interaction on skew plane, i.e. separation equal in the horizontal and vertical planes, and the analytical strength of the coupling Eq. 18. As expected, the agreement worsens for small separations since the analytical derivation assumes a long-range interaction.

3.4.2 IMPACT OF A ROLL ANGLE ERROR OF THE CROSSING ANGLE PLANE

We define the roll angle as the angle with which the crossing angle plane is tilted with respect to the horizontal plane, for instance a roll angle ϕ of 0° expresses that the crossing angle is in the horizontal plane while a ϕ =90° represents a crossing angle in the vertical plane. In Fig. 19 we test the validity of the implementation of the linear coupling within TRAIN as a function of the roll angle comparing the average linear coupling with the analytic expression Eq. 18. For this control test we just use one IP where the long-range interactions are taking place with null transverse separation at the IP. The head-on interaction has been cancelled in the IP, since the analytic formula Eq. 18 just holds for long-range interactions ($d > 5\sigma$), as we have seen in Sec. 3.4.1. Since we are assuming that all long-range interactions take place at a constant normalised distance Eq. 9, the analytical formula provides an upper bound of the estimation of the linear coupling, as it can also be appreciated in Fig. 19. The shadowed areas show the bunch by bunch spread around the average linear coupling.

The comparison between the analytical formula and the predicted linear coupling is good in this simplified case for both LHC and HL-LHC. We have used the number of long-range interactions up to D1 for both LHC and HL-LHC while using Eq. 18 to provide the analytical estimation of the linear coupling, since as it can be appreciated in Fig. 4 the assumption of constant normalised distance just holds up to D1.

In the following, we have analysed the linear coupling in a real configuration for both LHC and HL-LHC during collision. In the case of LHC we have considered the 2018 configuration at the end of the squeeze with the optics *opticsfile.22_ctpps2* [32] featuring a half crossing angle of 160 μrad and a β^* of 30 cm. The parallel separation bumps are set at 0.55 mm in IPs 1 and 5 and the vertical offset of 1.8 mm at IP5 compensating for the misalignment of the tunnel w.r.t. the CMS cavern is enabled. The linear coupling as a function of the roll angle in IP1 and IP5 is shown in Fig. 20. In the case of HL-LHC we have analysed the linear coupling dependence in the roll angles of IPs 1 and 5 in collision for the nominal and ultimate scenarios, when the separation bumps of IPs 1 and 5 have been already collapsed in Fig. 21. The different shapes of Figs. 20 and 21 can be explained with the different phase advance between IPs 1 and 5 which can make their contributions add up, as in the case of Fig. 21, or cancel Fig. 20.

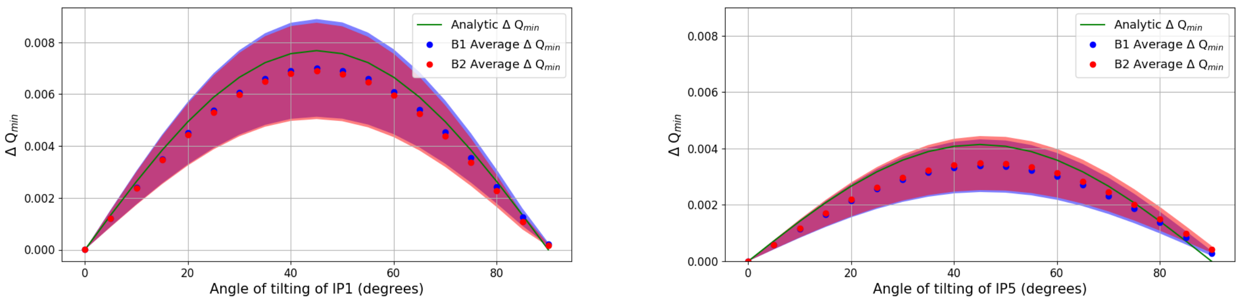

(a) LHC

(b) HL-LHC

Figure 19: Simulated average closest tune approach as a function of the analytical expression Eq. 18 for the nominal configuration of the HL-LHC at the start of collision and for LHC considering the 2018 configuration with the optics *opticsfile.22* [32] featuring a half crossing angle of 160 μrad and a β^* of 30 cm. The parallel separation bumps as well as the head-on interaction are disabled, thus matching the hypothesis behind the analytical derivation. The corresponding standard filling schemes were used. The shaded area represent the spread of the linear coupling within a beam. We note that the LHC configuration considered features a smaller normalised separation between the beams, due to the smaller β^* and crossing angle with respect to the HL-LHC nominal configuration.

As it can be observed in Figs. 19a and 20, a misalignment resulting in a roll angle in one IP between 10° and 15° or the combined misalignment of IPs 1 and 5 up to 15° would be compatible with the measured $|C^-|$ of around 2×10^{-3} to 3×10^{-3}, thus explaining the factor 10 in the closest tune approach that was measured during operation [26] with respect to the analytical formula Eq. 18 mentioned above.

We also observe on Figs. 21 and 20 that the linear coupling is not zero in absence of roll angle which is not predicted by the theory. This contribution comes from the orbit effect at the other IPs, generating an offset perpendicular to the crossing angle plane at the location of the long-range interactions resulting in a skew quadrupolar component. Since this contribution is not linked to a misalignment, but a PACMAN effect, its correction is not possible. A refined analysis of the effect is shown in Fig. 22 showing that the peak-to-peak PACMAN $|C^-|$ reaches 10^{-3} in ultimate scenarios at the end of the squeeze. Assuming that the machine can be corrected based on the nominal bunch, we may expect a remaining PACMAN contribution of $5{\cdot}10^{-4}$, representing half of the tolerance on linear coupling set for beam stability [33].
The additional contribution generated by a roll angle error of the crossing angle in a single IP exceeding 5° already exceeds the tolerance (Fig. 19). The combined effect of roll angle errors in IPs 1 and 5 is shown in Fig. 21. We note that a roll angle of 5° correspond to a crossing angle of 22 μrad in plane perpendicular to the crossing angle plane which is comparable to the uncertainty on the measurement obtained through K-modulation [31]. While in practice the misalignment of the orbit of the two beams at the location of the long-range interactions cannot be modelled with a simple roll angle, this example show that errors resulting in long-range interactions on a plane tilted by a few degree generates significant linear coupling and therefore requires a correction of the orbit at this level.

The first contribution discussed above is generated by a combination of an orbit effect scaling with $1/d$ (Eq. 7) and a coupling effect scaling with $1/d^2$ (Eq. 18), the overall effect therefore scales with $1/d^3$. Consequently a reduction of 50% is expected if collision is established at β^*=64 cm instead of 41 cm also in the operational scenario. The sensitivity to misalignments of the crossing angle scales with $1/d^2$, one may therefore expect a reduction of this contribution by 35% with the same increase of the β^* at the start of collision. Further increase is clearly beneficial for this effect. An additional reduction of

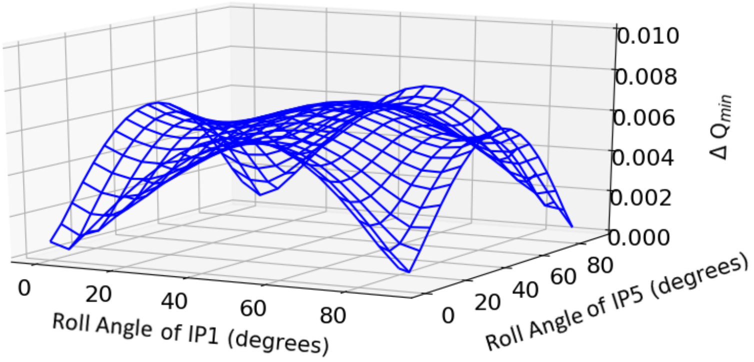

Figure 20: Simulated average closest tune approach as a function of the analytical expression Eq. 18 for LHC 2018 configuration (optics file *opticsfile.22_ctpps2*) using the Standard filling scheme. The results for B1 are shown, the behaviour is equivalent to the one of beam 2.

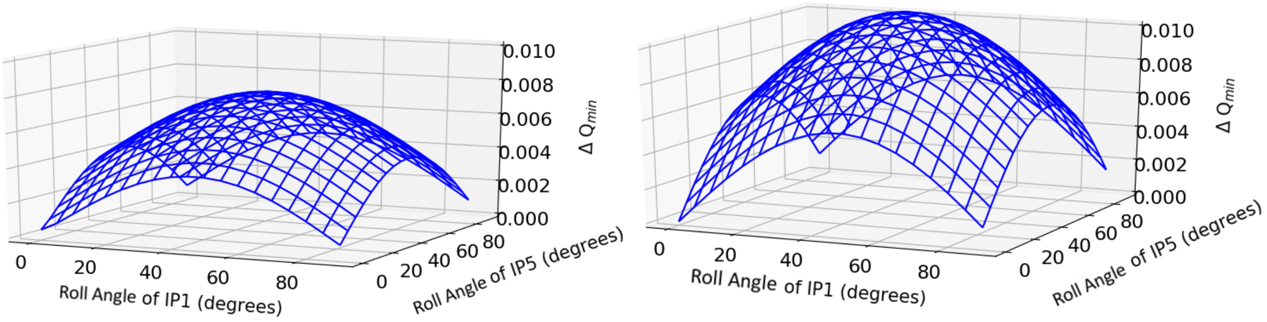

(a) Nominal scenario ($\beta^* = 64$ cm).

(b) Ultimate scenario ($\beta^* = 41$ cm).

Figure 21: Linear coupling dependence on the roll angle of IPs 1 and 5 for both the nominal and ultimate scenario in collision in HL-LHC. The results for B1 are shown, the behaviour is equivalent to the one of beam 2.

40 % and 30% of the two contribution discussed above can be obtained by increasing the crossing angle from 250 to 295 μrad, corresponding to the maximum compatible with the orbit correction scheme [34]. A further reduction of the contribution arising from the orbit effects at other IPs may be achieved through an optimisation of the phase advances between them to minimise the orbit effect at the long-range interactions.

3.4.3 DESIGN OF AN EXPERIMENT FOR PACMAN LINEAR COUPLING MEASUREMENT AT THE LHC

In the following, we detail a possible experiment that would allow to measure the PACMAN linear coupling respecting the constraints for the protection of the machine against beam induced damages. Our purpose is to validate our hypothesis that a misalignment of the orbit in the interaction region can explain the large discrepancy between measured and expected PACMAN linear coupling in the LHC.

Until now, the results presented have been computed varying the roll angle of both beams, so we could compare the behaviour of beam 1 and 2 with the analytical formula Eq. 18. However, in a real experiment tilting the roll angle for both beam 1 and 2 at the same time may challenge the required apertures in the triplet, since a large change in orbit would follow. In order to minimise the risk for the aperture we consider an asymmetric configuration in which the measurements and orbit movements are performed on a low intensity beam, here beam 1, colliding with bunch trains of the other beam, beam 2,

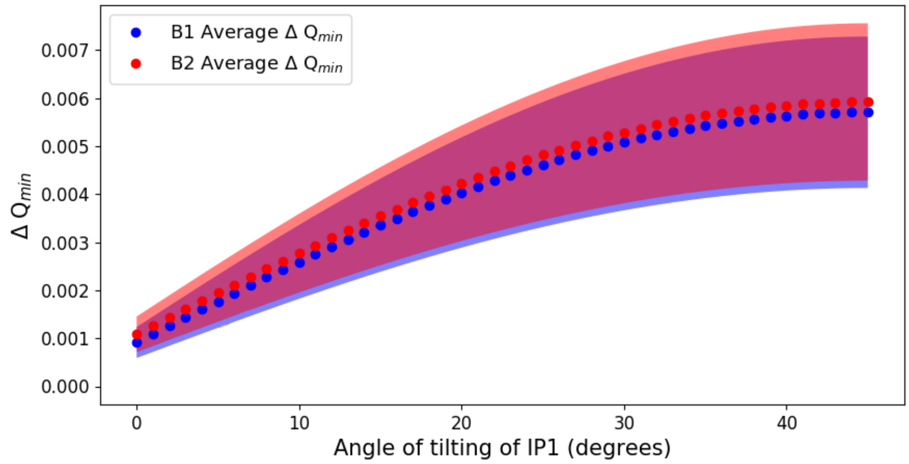

Figure 22: Simulated closest tune approach for beam 1 and 2 due to the long-range interactions in IPs 1 and 5 as a function of a roll angle error in IP5. The dots represent the values obtained for the nominal bunch while the shaded areas represent the spread among PACMAN bunches.

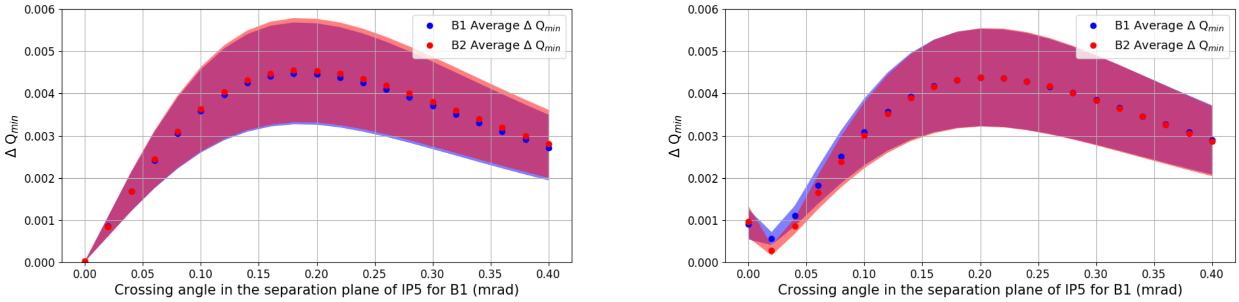

(a) Long-range interactions in IP5.

(b) Long-range interactions in IPs 1 and 5.

Figure 23: Minimum tune separation as a function of the crossing angle introduced in the parallel separation plane for beam 1 around IP5 for the experiments proposed in the LHC in 2018. All parallel and perpendicular separations have been eliminated and the head-on interactions are excluded from the computation.

for which the orbit is fixed.

As a control test, we simulate the effect of introducing a crossing angle in the separation plane up to 400 μrad without parallel separation nor vertical displacement correction for CMS (IP5). We have also deactivated the head-on interactions. In Fig. 23, the minimum tune separation is represented as a function of the crossing angle of the separation plane for B1 around IP5 with a full horizontal crossing angle of 320 μrad [32]. In Fig. 23a the long-range interactions just take place at the interaction region 5, while in Fig. 23b, we allow the long-range interactions in both IPs 1 and 5 while the crossing angle in the separation plane is only introduced in IP5. As it can be observed, the linear coupling in this simple configuration for 0 crossing angle in the separation plane is close to 0, since there is no other source of linear coupling, given that the horizontal and vertical separation have been collapsed. However, in Fig. 23b, the linear coupling for 0 crossing angle in the separation plane is already of the order of magnitude of 10^{-3}, even though the parallel and crossing angle plane separations in both IPs 1 and 5 have been eliminated. Indeed, this coupling is introduced due to the different crossing planes of both IPs where the long-range interactions are taking place, due to the orbit effect in IP1 that introduces a vertical component in the orbit at IP5 and vice-versa. It is also interesting to notice that the order of magnitude of the predicted linear coupling is 10^{-3}, which can be measured during an experiment.

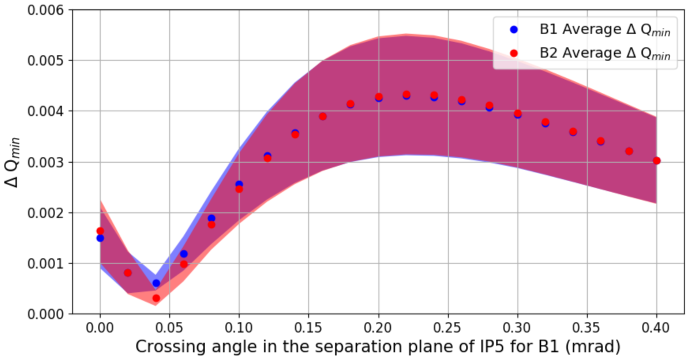

Figure 24: Minimum tune separation as a function of the crossing angle introduced in the parallel separation plane for beam 1 around IP5 for a realistic collision in LHC [32]. The full parallel separation has been set to 6σ in both IPs 1 and 5 in order to avoid the head-on interactions and a vertical separation of 1.8 mm in IP5 has been kept in order to account for the sink of CMS.

In Fig. 24, the linear coupling as a function of the crossing angle in the parallel plane for beam 1 is simulated for a realistic configuration for LHC. In order to avoid the head-on interactions, a full separation of 6σ has been introduced in both IPs 1 and 5 in the plane parallel to the crossing angle in the case of IP1 and in the crossing angle plane (vertical plane) in IP5. The vertical correction separation in IP5 of 1.8 mm has also been introduced. As it can be appreciated, for 0 crossing angle in the parallel plane, the linear coupling is even larger than for Fig. 23b, since the minimum tune separation in this configuration is not only given by the interplay of the long-range interactions in IPs 1 and 5, but also due to other sources of coupling such as the separation of the interacting beam at the IP.

According to Fig. 24, the maximum linear coupling can be reached for a crossing angle in the parallel separation plane of around 200 μm. While reasonable, detailed computations are required to assess the available physical aperture for such an orbit bump.

The linear coupling induced in these configurations is within the measurement accuracy and therefore could be used to validate the predictions of the model.

4 Conclusion

The bunch-by-bunch variations of orbit, tune and chromaticity are mostly within tolerances for both the nominal and ultimate scenarios. Nevertheless, the orbit effect of super-PACMAN bunches in the side experiments as well as non-colliding bunches in IPs 1 and 5 needs to be taken into account in the estimation of the aperture requirement in case of an asynchronous dump, since the constraint is imposed by the orbit of a small subset of consecutive bunches given by the kicker rise time. In order to deal with this shift we recommend to increase the protected aperture by 0.44 σ at top energy and 0.6 σ at injection energy. The first estimates of crab cavity loading due to PACMAN effects [12], which suggested that the overall contribution remains smaller than the uncertainty on the measured voltage in the cavity, were confirmed with the more accurate physics model developed. Also, the luminosity loss of the two high luminosity experiments due to the PACMAN orbit effects have been shown to be negligible, i.e. around 0.1% for both the nominal and ultimate scenarios with collision optics, once the re-optimisation of the orbit has been performed.

The tune spread introduced by the PACMAN effects is small enough such that its impact on the stability of single particle trajectories may be neglected. A chromaticity spread of 3 units was found arising from the combination of an uncorrected dispersion at the IP with the long-range driven offset at the IP plus the offset beam-beam interaction at the IP. Given its strong dependence on the transverse amplitude, its impact on dynamic aperture is expected to differ significantly from variations of chromaticity introduced with the lattice sextupoles and therefore should be addressed with dedicated simulations including residual dispersion at the IP as well as the offset at the IP due to PACMAN effect. The contribution to the chromaticity due to the PACMAN feed-down effect in the arc octupoles has been found to be negligible.

The linear coupling variations were identified as potential issue to maintain the beam stability. To describe this effect accurately, the computation of linear coupling induced by beam-beam interaction on skew plane was implemented in TRAIN and used to analyse the LHC 2018 and HL-LHC configurations. In particular, it was found that the first measurement of PACMAN coupling performed in the LHC are compatible with the expectation, taking into account the skewing of the long-range interactions by the beam-beam induced orbit effect at the other IPs as well as by potential misalignments of the crossing angle plane.

Since this effect depends strongly on the alignment of the crossing angles bumps in the different IPs, its control will rely on measurement and correction of the orbit in the interaction region, requiring a control of the crossing angle perpendicular to the crossing plane in the order of 10 μrad.

Based on these considerations, we conclude that the effect of PACMAN linear coupling and the corresponding correction tolerance should be studied experimentally. In case this effect can not be controlled to the required level, a reduction of the normalised separation between the beams at the start of collision should be envisaged through an increase of crossing angle, β^* or both.

Acknowledgments

The authors would like to thank A. Gorzawski and M. Hostettler for their important contributions to the TRAIN code, as well as R. Bruce and R. De Maria for their input on the estimation of the impact on the physical aperture and R. Calaga for fruitful discussions on crab cavity loading.

This research was supported by the HL-LHC project.

References

[1] W. Herr, *Features and implications of different LHC crossing schemes*, CERN, Geneva, Switzerland, LHCProjectReport628, 2003.

[2] H. Grote, *Self−Consistent orbits with Beam−Beam interactions in the LHC*, Proceedings of EPAC, 2000.

[3] S. Antipov, F. Antoniou, R. Appleby, G. Arduini, J. Barranco, P. Baudrenghien, N. Biancacci, C. Bracco, R. Bruce, X. Buffat, R. Calaga, L.R. Carver, M. Crouch, R. De Maria, S. Fartoukh, D. Gamba, M. Giovannozzi, P. Goncalves Jorge, W. Höfle, G. Iadarola, N. Karastathis, A. Lasheen, K. Li, T. Mastoridis, L. Medina, A. Mereghetti, E. Métral, D. Mirarchi, B. Muratori, S. Papadopoulou, Y. Papaphilippou, D. Pellegrini, T. Pieloni, S. Redaelli, G. Rumolo, B. Salvant, E. Shaposhnikova, M. Solfaroli-Camillocci, C. Tambasco, R. Tomás, D. Valuch, *Update of the HL-LHC operational scenarios for proton operation*, CERN, Geneva, Switzerland, CERN-ATS-Note-2018, 2018.

[4] X. Buffat, *Coherent Beam−Beam Effects*, CERN, Geneva, Switzerland, CERN-2017-006-SP, 2017.

[5] E. Keil, *Truly Self-Consistent Treatment of the Side Effects with Bunch Trains*, CERN SL/95-75 (AP), Geneva, Switzerland, 1995.

[6] M. Hostettler, *LHC Luminosity Performance*, CERN-THESIS-2018-051, Geneva, Switzerland, 2018.

[7] A. Gorzawski, *Luminosity control and beam orbit stability with beta star leveling at LHC and HL-LHC*, EPFL, 2016 (CERN-THESIS-2016-193).

[8] Train TWiki, `https://twiki.cern.ch/twiki/bin/view/ABPComputing/TrainWikiPage`.

[9] A.W. Chao and M. Tigner, *Handbook of Accelerator Physics and Engineering*, World Scientific, Singapore, 1999.

[10] S. White, *Determination of the absolute luminosity at the LHC*, Ph.D. thesis, Université Paris-Sud (2010).

[11] F. Follin, R. Alemany-Fernandez, R. Jacobsson, *Online luminosity optimization at the LHC*, Proceedings of ICALEPCS2, CERN, Geneva, Switzerland (2013).

[12] E. Yamakawa, P. Baudrenghien, R. Calaga, R. Apsimon, and A. C. Dexter, *Crab cavity studies including full detuning and offsets due to long range beam-beam interactions*, Presented at the 7th HL-LHC Collaboration Meeting, Madrid, Spain, `https://indico.cern.ch/event/647714/contributions/2768967/attachments/1557095/2449950/wp4-crab-cavity.pdf`.

[13] H. Grote and W. Herr, *Nominal and ultimate luminosity performance of the LHC*, LHC Project Note 275, Geneva, Switzerland, 2002.

[14] X. Buffat, *PyLumi*, `https://gitlab.cern.ch/xbuffat/PyLumi`.

[15] R. Bruce, C. Bracco, R. De Maria, M. Giovannozzi, S. Redaelli, R. Tomas Garcia, F. M. Velotti, and J. Wenninger, *Updated parameters for HL-LHC aperture calculations for proton beams*,CERN- ACC-2017-0051 (CERN, Geneva, 2017).

[16] R. Bruce, R. W. Assmann, and S. Redaelli, *Calculations of safe collimator settings and β^* at the CERN Large Hadron Collider*, Phys. Rev. ST Accel. Beams, vol. 18, p. 061001, Jun 2015.

[17] X. Buffat, L. Barraud, E. Métral, A. Ribes Metidieri, J. Barranco, P. Gonçalves, T. Pieloni and C. Tambasco, *Status of the studies on collective effects involving beam-beam interactions at the HL-LHC*, CERN-ACC-NOTE-2018-0036 (CERN, Geneva, 2018).

[18] W. Scandale, *Dynamic aperture*, CERN, Geneva, Switzerland (1993).

[19] N. Karastathis, S.Kostoglou, Y. Papaphilippou, K. Skoufaris and G. Sterbini, *Long-range compensation: PACMAN and HO impact in HL-LHC dynamic aperture*, Presented at the 120th HL-LHC work package 2 meeting `https://indico.cern.ch/event/726041/contributions/2987311/attachments/1645893/2630457/WP2_08_05_2018.pdf`.

[20] R.Tomás private communication, July 2018.

[21] B. Erdélyi and T. Sen, *Analytic Studies of the Long Range Beam-Beam Tune Shifts and Chromaticities*, FERMILAB-TM-2171 (FERMILAB, Batavia, IL 60510, 2002).

[22] D. Pellegrini, S. Fartoukh, N. Karastathis, Y. Papaphilippou, *Multiparametric response of the HL-LHC dynamic aperture in the presence of beam-beam effects*, CERN, Geneva, Switzerland, Proceedings of IPAC 2017.

[23] S. Fartoukh, *Achromatic telescopic squeezing scheme and application to the LHC and its luminosity upgrade*, Phys. Rev. ST Accel. Beams, vol. 16, p. 111002, Nov 2013.

[24] X. Buffat, W. Herr, N. Mounet, T. Pieloni and S. White, *Stability diagrams of colliding beams in the Large Hadron Collider*, Physical review special topics- accelerators and beams 17 (2014).

[25] L.R. Carver, D. Amorim, N. Biancacci, X. Buffat, K.S.B. Li, E. Métral, B. Salvant, M. Schenk, *Desestabilising effect of linear coupling in the LHC*, CERN, Geneva, 2017.

[26] J. Wenninger, X. Buffat, F. S. Carlier, J. M. Coello De Portugal Martinez Vazquez, K. Fuchsberger, M. Hostettler, T. H. B. Persson, R. Tomas Garcia, D. Valuch, and A. Garcia-Tabares Valdivieso, *LHC MD2877: Beam-beam long range impact on coupling measurements*, CERN-ACC-NOTE-2018-0026 (CERN, Geneva, Switzerland, 2018).

[27] F. Ruggiero, G. Rumolo, F. Zimmermann and Y. Papaphilippou, *Beam Dynamics Studies for Uniform (Hollow) Bunches or Super-bunches in the LHC: Beam-beam effects, Electron Cloud, Longitudinal Dynamics, and Intrabeam Scattering*, LHC-Project-Report-627 (CERN, Geneva, 2003).

[28] W. Fischer, *Robust linear coupling correction with N-turn maps*, Brookhaven National Laboratory, Upton, USA (2003).

[29] L. Deniau, *Methodological Accelerator Design. Highlights on Coupling Calculations. Part I - Initialization*, Presented on BE/ABP-HSS meeting `https://indico.cern.ch/event/672801/contributions/2752703/attachments/1546876/2461487/ld_20171025-HSS.pdf`, Geneva, Switzerland (2017).

[30] D. Sagan and D.Rubin, *Linear analysis of coupled lattices*, Wilson Laboratory, Cornell University, Ithaca (1999).

[31] L. van Riesen-Haupt, A. Seryi, R. Tomàs, J.M. Coello de Portugal and E. Fol, *K-Modulation developments via simultaneous beam based alignment in the LHC*, Proceedings of IPAC2017, Copenhagen, Denmark

[32] LHC 2018 optics repository */afs/cern.ch/eng/lhc/optics/runII/2018/PROTON*.

[33] X. Buffat, et al., *Strategy for Landau damping of head-tail instabilities at top energy in the HL-LHC*, CERN-ACC-2019, in preparation

[34] R. De Maria, D. Gamba, and F. Plassard, *HL-LHC V1.4,* Presented at the HL-LHC Technical Coordination Committee Meeting, CERN, Geneva, `https://indico.cern.ch/event/758028/contributions/3143207/attachments/1719731/2775919/`, HL14-TCC3.pdf (20th Sept. 2018)